An Experimental Investigation of the Impedance of Coupled Multistable Structures Subjected to Harmonic Excitation

Undergraduate Honors Thesis

Presented in Partial Fulfillment of the Requirements for Graduation with
Honors Research Distinction in the Department of Mechanical and Aerospace Engineering
of The Ohio State University

By

Benjamin A. Goodpaster

Undergraduate Program in Mechanical Engineering

The Ohio State University

April 2017

Thesis Committee:
Ryan L. Harne, Advisor
Jack McNamara

ABSTRACT

Reliable aircraft components capable of operating in the extreme conditions of hypersonic flight have wide-ranging applications in the development of future commercial and defense air vehicles. A major obstacle to this objective is that the thin skin panels that compose aircraft structures may warp into states with multiple static equilibria. These panels may then exhibit snap-through, or high-amplitude oscillations between static equilibria, in consequence to the mechanical, thermal, and acoustical loads experienced by aircraft traveling at hypersonic speeds. This "skin buckling" phenomenon permanently deforms airframe panels, leads to decreased flight performance characteristics, increases wear on structural components, decreases structure life, and may result in catastrophic failure. While the steady-state dynamics of single degree-of-freedom bistable structures have been well characterized, it is unclear how to generalize this knowledge to a complex multistable structure, such as a post-buckled aircraft panel, having multiple degrees-of-freedom. To gain a fundamental understanding of multistable structures operating in extreme environments, this research experimentally investigates an archetypal, built-up multistable structure that consists of coupled, bistable beams. Experimental parametric studies are conducted on multiple configurations of this archetypal structure to uncover relationships among excitation features and mechanical impedance. The results of this research are used to articulate a new method of experimental investigation of multistable structures that may be used to forecast dynamic regime changes that may manifest in built-up aerostructures operated in the extreme conditions of hypersonic flight.

ACKNOWLEDGEMENTS

I first want to thank my advisor, Prof. Ryan L. Harne. I would never have been able to complete this research without his constant guidance and support.

I also wish to thank Prof. Jack McNamara for his help as my committee member.

Finally, I would like to acknowledge support from the U.S. Department of Defense Science, Mathematics, and Research for Transformation (SMART) Scholarship and from the OSU College of Engineering Honors Research Scholarship.

All experiments presented in this research were conducted in the Laboratory of Sound and Vibration Research (LSVR), which is directed by Dr. Harne.

TABLE OF CONTENTS

LIST OF FIGURES

LIST OF TABLES

1 INTRODUCTION

1.1 Motivation

One major hindrance to the development of hypersonic aircraft has been the onset of multistability of structural components due to a combination of geometric features and the extreme operational environment of hypersonic flight [1]. For example, modern aircraft employ thin, slender components on wings, control surfaces, and fuselage in order to maximize fuel efficiency and improve maneuverability [2] [3]. Due to the combined mechanical, thermal, and acoustical loading that aircraft are routinely subjected to during operation, these slender components may be stressed to an extent to cause *skin buckling*, which is the warping of panels into *multistable* configurations between stiffened components, such as ribs or rivets. This skin buckling phenomenon has been observed on the SR-71 Blackbird, a hypersonic reconnaissance aircraft designed by Lockheed Martin during the height of the Cold War [4], shown in Figure 1(a). Skin buckling has also been shown to exist outside the realm of hypersonic flight, as exhibited by the most recent iteration of the Boeing B52 Stratofortress [5] shown in Figure 1(b).

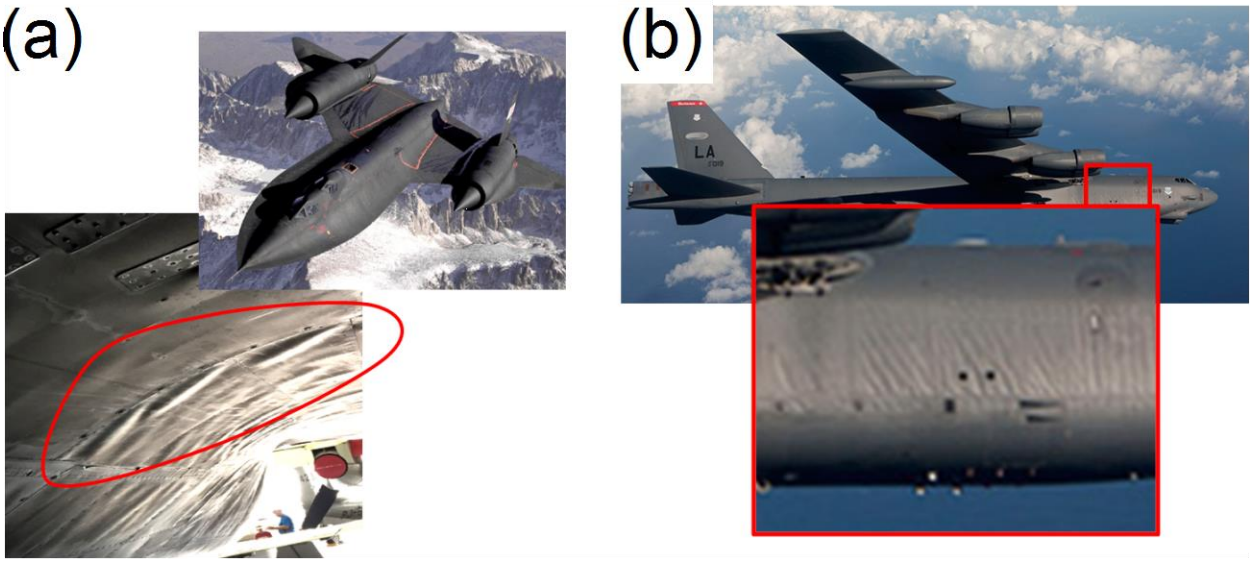

Figure 1. Examples of skin buckling. (a) SR-71 Blackbird underbelly; (b) recent generation of Boeing B52 Stratofortress.

Multistability in a mechanical system refers to the property of having multiple stable equilibrium configurations. *Snap-through* is the steady-state dynamic response associated with large-amplitude oscillations between the static equilibria of a multistable structure. Also termed an 'interwell' response, snap-through is a nonlinear dynamic characterized by a sudden conversion between the potential and kinetic energy of a system [6]. Figure 2 shows an example of the potential energy-displacement relationship of a bistable structure, the simplest example of multistability that exhibits two stable static equilibria. Snap-through occurs when the total energy of the system exceeds the energy barrier corresponding to the unstable equilibrium (red circle) and transitions between the local potential energy wells, the minima of which correspond to the stable static equilibrium positions (green and blue squares). When the total energy of the

system is less than that necessary to induce snap-through, an 'intrawell' dynamic response occurs that is quasi-linear for small-amplitude oscillations.

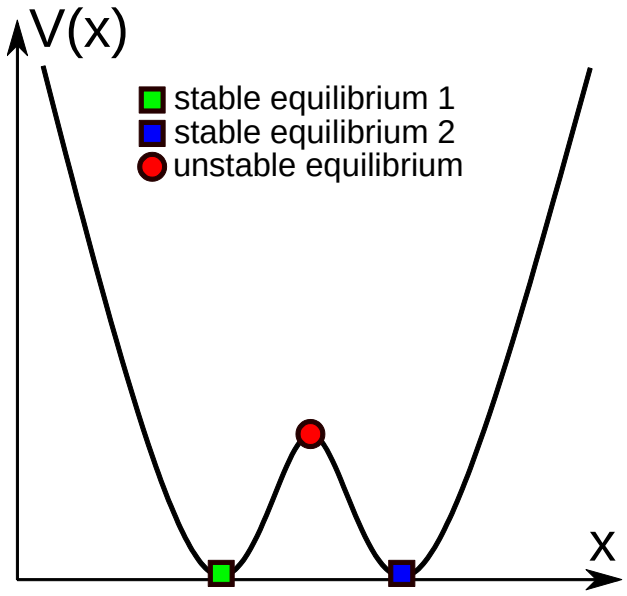

Figure 2. Bistable system potential energy-displacement relationship.

Depending on system parameters, multistable structures can exhibit coexistent dynamic regimes for certain excitation features. Under these conditions, small system perturbations in the form of impulsive forces or variations in excitation frequency or amplitude can trigger a transition between a low-amplitude intrawell response and high-amplitude snap-through. Figure 3 displays this transition occurring in a bistable system due to a manual impulsive force. The bistable system considered in Figure 3 consists of a simply-supported beam that has been axially compressed to induce buckling. The beam is subjected to a constant amplitude harmonic excitation force with a slowly varying drive frequency at a rate of 0.16 Hz/s. The impulsive force is applied by quickly yet lightly impacting the beam center, which causes the beam to suddenly transition into a high-amplitude snap-through response.

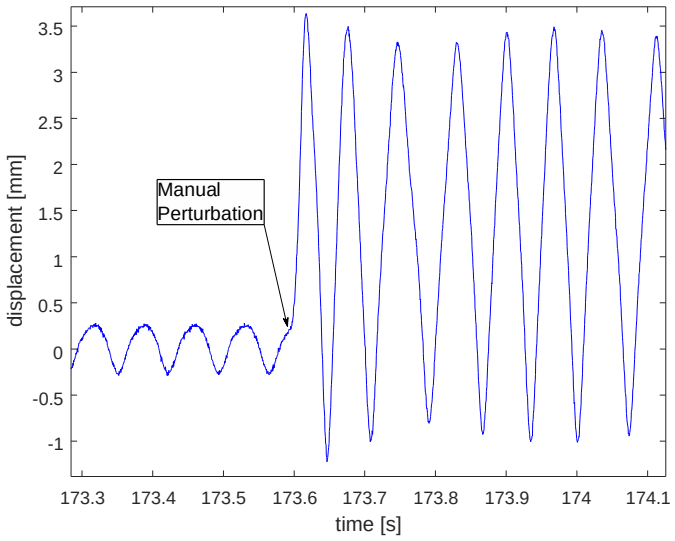

Figure 3. Transition between intrawell and snap-through response of a bistable system due to a manual perturbation, occurring at approximately 173.6 [s].

On aircraft, multistability can become manifest in the form of skin buckling. The onset of multistability can be severely detrimental to the operational performance of hypersonic vehicles due to the significantly increased variation of drag and lift created by the non-smooth surfaces while the structural integrity is simultaneously compromised by the additional stresses associated with dynamic snap-through between multiple stable states. The sudden transition between low- and high-amplitude dynamic responses that characterizes the onset of snap-through can reduce fatigue life and cause severe structural damage to aircraft panels. Thus, the ability to predict the onset of high-amplitude dynamic responses is of significant practical importance. This research focuses on utilizing mechanical impedance metrics in order to predict the onset of a change in the dynamic regime of response.

1.2 Mechanical impedance

In electrical circuits, impedance is a complex number that dictates how energy transfers through an electrical system. It is the complex ratio of the *potential* (voltage) to the *flow* (current) in a circuit. The real part of the impedance is the *resistance* while the imaginary part is the *reactance*. The resistance denotes the effectiveness of energy transfer among system components (or dissipation, for single degree-of-freedom systems), while the reactance denotes the effectiveness of reciprocal energy exchange among system components. Analogously, *mechanical impedance* is the complex ratio of the potential (force) to the flow (velocity) in a mechanical system and determines a component's ability to transfer and dissipate energy [7]. The interpretations of resistance and reactance components of mechanical impedance are analogous, respecting the electrical counterparts. Mechanical impedance is determined by comparing the amplitude and phase of a force acting on a system at a point to the amplitude and phase of velocity of a component at another point. If the force and velocity are measured at the same location, the result is referred to as a *drive-point impedance*, while measurements from different locations result in a *transfer impedance* value.

Impedance has been used for decades in the study of linear structural dynamics [8], while more recent investigations have considered how to extend the concept to nonlinear structural dynamics involving relatively weak nonlinear behaviors [9] [10] [11] [12]. Yet, an understanding of the far-from-equilibrium, strongly nonlinear dynamics of multistable structures remains outstanding, so that relevant impedance metrics for such characteristic behaviors have not been articulated.

1.3 State-of-the-Art

Researchers have sought to characterize the harmonic and stochastic responses of individual bistable beam structures induced in consequence to excitation forces and loads. The similarities between this archetypal platform and a more general multistable structure composed of many such fundamental post-buckled constituents assist in more straightforward theoretical and computational work by giving attention to the archetypal constituents. For example, Wiebe et al. [13] investigated the snap-through dynamics of a single degree of freedom Duffing-type oscillator in order to understand the circumstances that lead a multi-degree-of-freedom (DOF) curved structure to exhibit large amplitude, snap-through buckling. Indeed, the dynamic responses of bistable structures and analytical methods to examine them are both well documented and established [14] [15].

On the other hand, real aircraft are assembled from many beam or panel constituents, such that the overall dynamic response of one panel is inherently related to those of its neighbors [16]. These more complicated structures are well-known to be strongly coupled and complex at the onset of buckling and have the potential to exhibit cascading nonlinear dynamic responses [17]. To study complex structures directly, high-fidelity models are usually developed and evaluated using finite element (FE) or reduced order methods. However, the mass, stiffness, and damping constants that FE software use to solve for structural dynamics must be accurately identified, a task that is difficult due to the presence of nonlinearities. Methods for determining the necessary constants have been described by Spottswood and Allemang [18] [19] and delli Carri and Ewins [20], while new experimental methods using laser- and high-speed-video-based methodologies are producing new procedures for obtaining these necessary structural parameters. These methodologies are opening new pathways for the exploration of the nonlinear dynamics of multistable structures, while reduced order modeling has been shown to further increase the efficiency of these simulations [21]. In addition, these methods are readily expanded to include such phenomena as thermal buckling of panels subjected to acoustical loads [22] as well as thermal-structural coupling between aircraft panels and hypersonic fluid flow [23]. While this avenue of investigation is making substantial gains, it is still a computationally and time-consuming operation which is only relevant for the specific parameters being modeled, making extensive parametric studies burdensome and time-consuming.

1.4 Problem statement

In order to bridge the knowledge gap between the analytical and computational approaches, the authors have recently developed a semi-analytical method that identifies the impedance metrics of multistable structures as a method to gain fundamental insight into the complex dynamic behavior of such structures [7]. This framework has been developed in order to analytically characterize how energy transfers through

built-up, multi-DOF multistable structures in dynamic steady-states, and has successfully predicted different classes of far-from-equilibrium, snap-through dynamics. However, it is unclear how impedance metrics of multistable structures behave as these structures undergo rapid changes is dynamic steady-state. The proposed framework [7] promises to provide valuable insight into these trends. However, no extensive experimental evidence of the mechanical impedance trends of built-up multistable structures presently exists that can serve as a baseline for verifying results from this model.

1.5 Research goal

The goal of this research is to experimentally identify trends in the mechanical impedance of multistable structures subjected to harmonic excitations to determine correlations between impedance characteristics and *bifurcations*, or sudden changes in dynamic regime. To achieve this goal, an archetypal multistable structure is designed and fabricated consisting of three coupled, bistable beams. Then, experiments are conducted to investigate the dynamic response of such a built-up multistable structure. The real-time impedance measurements of the beams are then evaluated to uncover trends corresponding with dynamic regime changes.

1.6 Overview of thesis

This thesis is organized as follows. Chapter 2 details the experimental setup of the archetypal multistable structure and describes the governing equations of motion for this system. Chapter 3 describes the data acquisition equipment and testing methods used in this investigation, and details the structural parameters of the multistable configurations considered. Chapter 4 presents typical experimental results and discusses the important trends observed in measured impedances. Chapter 5 summarizes these trends and proposes potential avenues for future investigation.

2 ARCHETYPAL MULTISTABLE STRUCTURE

2.1 Built-up multistable structure of coupled, post-buckled beams

A typical experimental platform to investigate bistable dynamics is a beam that has been axially-compressed to an extent to induce buckling [15]. If the beam is only lightly buckled, then only the first buckling mode becomes manifest and the beam may be considered a bistable structure. If two or more bistable beams are coupled together, this produces a multistable structure that has static configurations consisting of various combinations of the individual bistable beam static equilibria. Similarly, this research examines a multistable structure consisting of three simply-supported, post-buckled beams, shown in Figure 4(a), which has been designed and fabricated explicitly for this research. From here on, the beams will be referred to as beam 1, 2, and 3, as labeled in Figure 4(a). Each spring steel beam (E=200 GPa, I=4.0648×10^{-13} m^4, ρ=7800 kg/m^3, L=260 mm) is simply-supported via aluminum mounts with bearings at both beam ends. The bistability of each beam is controlled via an adjustable, fine-threaded load screw that moves one end of the beam in the axial direction with a high degree of precision, allowing each beam to be independently buckled to various degrees, shown in Figure 4(b). To excite the system, the center of beam 1 is connected to an electrodynamic shaker via a pair of tension springs as shown in Figure 4(c). The tension springs are connected to beam 1 via small, neodymium magnets that are lumped in to the effective mass of the beam. Each beam is connected to the subsequent beam via a pair of bent leaf springs, each with a thickness of 0.127mm, which act as linear coupling springs between beams. Each coupling spring interfaces with the beams due to a pair of small, square neodymium magnets, which can also be seen in Figure 4(a).

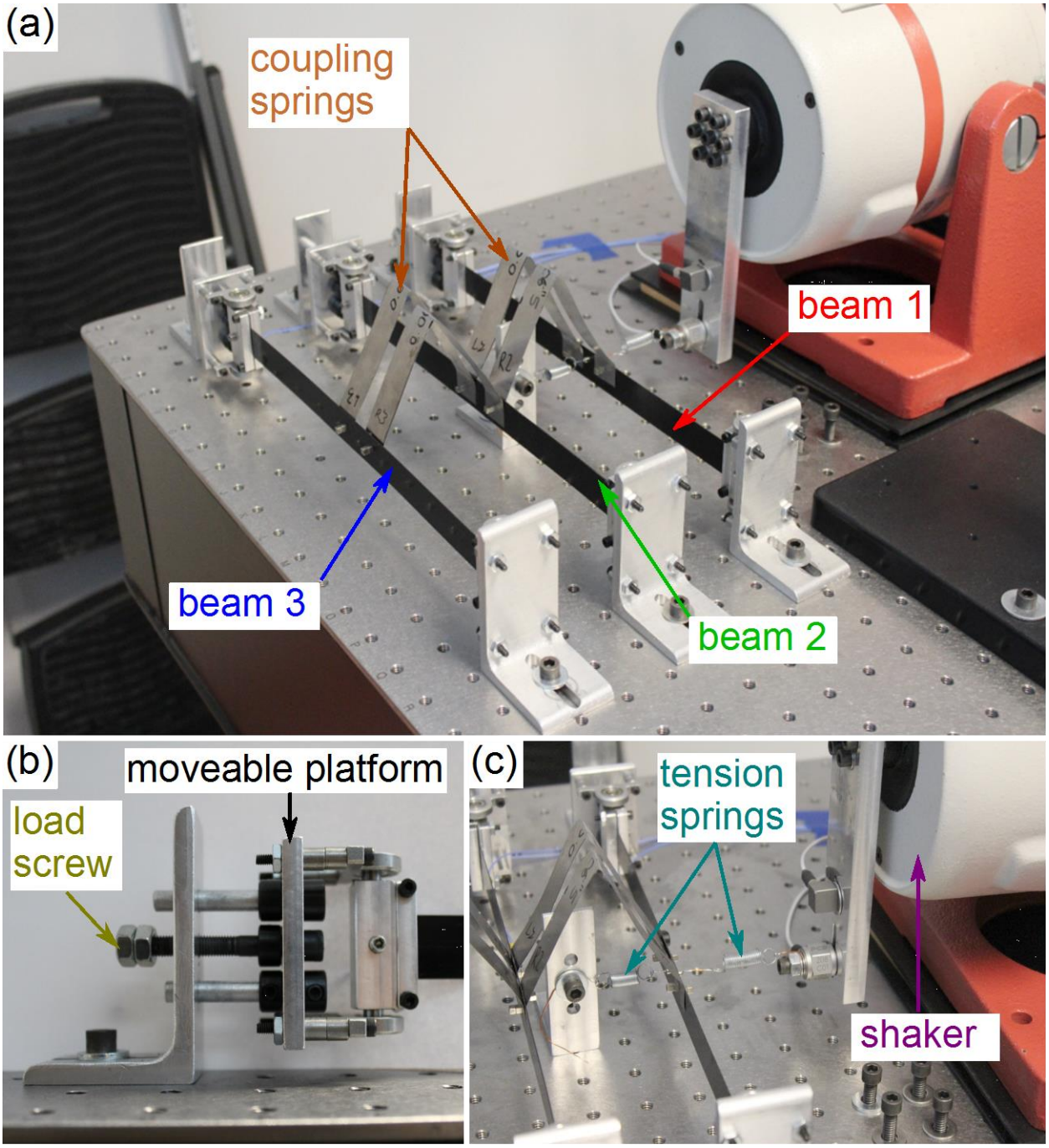

Figure 4. Experimental platform. (a) beams 1, 2, and 3 are coupled together via bent leaf springs; (b) moveable platform which supplies axial compression to individually buckle beams; (c) pair of tension springs connecting beam 1 to the electrodynamic shaker.

This experimental system provides a platform that is a low order representation of the more complicated case of the skin buckling phenomenon. Each individually buckled beam represents an aircraft panel that has been buckled due to local thermal, mechanical, and geometric effects. The leaf springs coupling adjacent beams is comparable to the stiffened components, such as rivets and ribs, which break up

continuous aircraft panels. The harmonic excitation from the electrodynamic shaker is representative of the mechanical and thermal loads that act on an aircraft structure during operation. Thus, this system provides a simplified representation of the skin buckling phenomenon from which to evaluate multistable structural impedance characteristics.

The beams considered in this research are lightly buckled, since the maximum distance between static equilibria of the beams without coupling springs was observed to be 3 mm, in contrast with the overall beam length of 260 mm. Thus, only the fundamental buckling modes became manifest, resulting in a 3DOF system.

2.2 Governing equations for lumped-parameter model

The governing equation of motion for the i^{th} beam in an *n* DOF system with adjacent beams coupled together is previously derived as [7]:

$$m_i\ddot{x}_i + b_i\dot{x}_i + k_{L,i}(1-p_i)x_i + k_{NL,i}{x_i}^3 - k_{c,i-1,i}(x_{i-1}+x_i) - k_{c,i+1,i}(x_{i+1}+x_i) = F_i\cos(\omega_i t) \quad (1)$$

where, x_i, m_i, b_i, $k_{L,i}$, and $k_{NL,i}$ are the beam center displacement, effective mass, viscous damping, linear stiffness, and nonlinear stiffness of the i^{th} beam, respectively, while $k_{c,i\pm1}$ is the linear coupling stiffness between adjacent beams. The load parameter p_i indicates the degree to which the beam is buckled, and whether the beam is pre- (p_i < 1) or post-buckled (p_i > 1). The harmonic excitation on each beam is characterized by the forcing amplitude F_i and excitation frequency ω_i. For the 3DOF system considered here, $k_{c,0,1} = k_{c,4,1} = 0$ and only beam 1 is subject to harmonic excitation, resulting in the following set of three coupled, ordinary differential equations:

$$m_1\ddot{x}_1 + b_1\dot{x}_1 + k_{L,1}(1-p_1)x_1 + k_{NL,1}{x_1}^3 - k_{c,2,1}(x_2+x_1) = F\cos(\omega t) \quad (2)$$

$$m_2\ddot{x}_2 + b_2\dot{x}_2 + k_{L,2}(1-p_2)x_2 + k_{NL,2}{x_2}^3 - k_{c,1,2}(x_1+x_2) - k_{c,3,2}(x_3+x_2) = 0 \quad (3)$$

$$m_3\ddot{x}_3 + b_3\dot{x}_3 + k_{L,3}(1-p_3)x_3 + k_{NL,3}{x_3}^3 - k_{c,2,3}(x_2+x_3) = 0 \quad (4)$$

Equations 2-4 indicate that the configuration of each beam while not coupled to adjacent beams is determined by five parameters, namely the mass, viscous damping, local linear stiffness, local nonlinear stiffness, and load parameter, referred to here as the *state* of the beam. These equations also indicate that two parameters determine the coupling strength between adjacent beams, noting that $k_{c,1,2} = k_{c,2,1}$ and $k_{c,2,3} = k_{c,3,2}$. The values of these seven parameters will be evaluated in the following chapter.

3 EXPERIMENTAL METHODS

3.1 Sensors, equipment, and data acquisition methods

The experimental platform is mounted on an optical isolation table (Newport Smart Table UT2), seen in Figure 4. A thick aluminum bar is mounted to the electrodynamic shaker (LDS V408) in order to transfer the motion of the shaker down to the midpoint of the beams. An accelerometer (PCB 333B40) and force transducer (PCB 208C01) are mounted to this bar in order to measure the input acceleration and input force into beam 1, respectively, shown in Figure 5(a). One accelerometer (PCB 352A24) is attached near the center of each beam in order to measure their dynamic responses, shown in Figure 5(b). The signals from all five sensors are fed into one of two signal conditioning boxes (PCB 482C05), which are connected to a data acquisition system (NI PXIe-1073, PXIe-6368). The shaker is controlled by a controller (Vibration Research VR9500) which uses the reference accelerometer on the shaker to create a feedback loop to precisely control the shaker output.

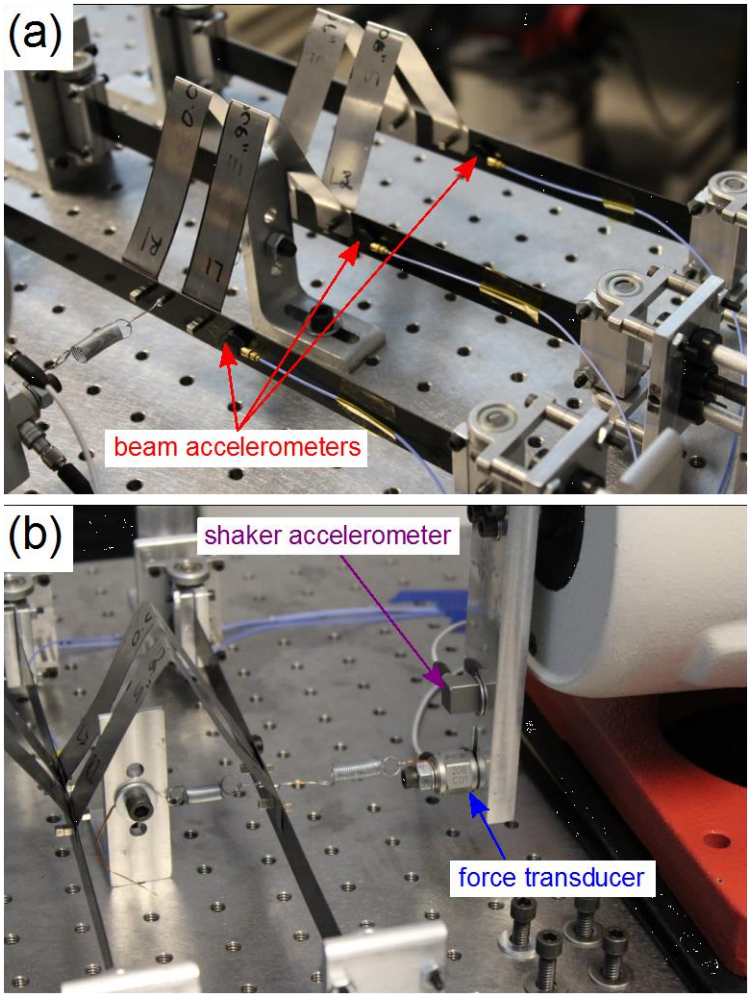

Figure 5. Photograph of sensors used to capture data during experimentation. (a) accelerometer and force transducer to measure shaker input; (b) accelerometers attached to each beam to measure dynamic response.

The MATLAB data acquisition toolbox is used to record all data from the sensors. The maximum excitation frequency considered is 30 Hz, so a minimum sampling rate of 300 Hz is required to accurately sample a sinusoidal waveform. On the other hand, higher-order harmonics are likely to occur which requires a sampling rate around 50 to 100 times the frequency of interest. Therefore, all tests are conducted with a sampling rate of 2048 Hz. Once the data is collected, all signals are digitially filtered through a bandpass filter between 1 Hz and 200 Hz. After this, the data is post-processed to calculate frequency response, amplitude response, and impedance plots. To achieve this, a fast Fourier transfrom is computed on the collected sets of data to convert the recorded data from time domain to frequency domain. Once in the frequency domain, the acceleration response amplitudes are numerically integrated by dividing by the angular excitation frequency to calculate beam center velocities, which are necessary for the subsequent impedance calculation. An example of this MATLAB code is provided in the Appendix.

3.2 Excitation parameters

Only harmonic excitations are considered in this research since they are the simplest excitation to realize and model while still providing rich insights into multistable structural dynamics. Harmonic waveforms are characterized by two parameters: frequency and amplitude. Therefore, in order to study the impact each of these parameters has on the dynamic response of the system, two categories of test are conducted. Harmonic frequency sweeps are conducted, during which the excitation amplitude is held constant and the frequency is slowly swept from 10 Hz to 30 Hz, 400 seconds up and 400 seconds down at a rate of 0.05 Hz/s. This slow sweep rate is chosen in order to realize only steady-state responses, while sweeping in both directions allows for the identification of potentially coexistent responses occurring at the same harmonic frequency. For every structural configuration, these harmonic frequency sweeps are nominally conducted at 0.5 m/s^2, 1 m/s^2, 3 m/s^2, 5 m/s^2, and 7 m/s^2 in order to observe responses ranging from quasi-linear to consistent system snap-through.

Harmonic amplitude sweeps are also conducted, during which the excitation frequency is held constant while the amplitude is slowly swept from 0.25 m/s^2 to 7 m/s^2, 300 seconds up and 300 seconds down at a rate of 0.0113 $m/s^2/s$. The frequencies at which these tests are conducted are chosen based on the observed coexistent responses between the different harmonic frequency sweeps, and typically include excitations in the 10 Hz to 13 Hz range, where system-level snap-through is observed at high amplitudes, and 15 Hz to 20 Hz, where nonlinear resonances are typically observed to occur. Table 1 provides a summary of the excitation parameters considered in this investigation.

Table 1. Summary of two different kinds of harmonic excitation sweeps.

Test Type	Input Harmonic Amplitude	Input Harmonic Frequency	Total Sweep Time	Sweep Rate
Harmonic Frequency Sweep	Nonzero constant	Slow sweep 10-30 Hz	400 seconds up 400 seconds down	0.05 Hz/s
Harmonic Amplitude Sweep	Slow sweep 0.25-7 m/s^2	Nonzero constant	300 seconds up 300 seconds up	0.0113 $m/s^2/s$

3.3 Structural parameters

As the governing equations in Section 2.2 demonstrate, there are five structural parameters that characterize the state of each beam, leading to a total of 17 parameters that completely define the system, including the coupling springs between adjacent beams. Any set of these 17 parameters is referred to in this research as a *configuration.* In order to ensure that observed impedance trends are representative of a variety of structural dynamic systems governed by Equations 2-4, three configurations are considered in this research, referred to as configurations 1, 2, and 3. In this way, the use of multiple configurations ensures that the empirical observations are repeatable for a variety of parameter combinations in the nonlinear, multistable platform. The configuration parameters are determined through an extensive system identification process, utilizing both mechanics and the measured natural frequencies and damping ratios of each beam.

To measure the natural frequency and damping ratio of each beam, the coupling springs between beams are removed and ring-down tests are conducted on each beam, wherein a manual impulsive force is applied via a rapid yet mild impact from one's finger at the beam's center and the dynamic response is recorded. An example of one such ring-down test is shown in Figure 6. The free-response of these bistable beams first begins with a highly nonlinear response as they transition between both equilibrium positions, before transitioning into the linear ring-down response associated with traditional underdamped, linear systems. The method of logarithmic decrement is utilized in this later, linear regime in order to calculate the natural frequency and damping ratio of each beam for each configuration. Table 2 summarizes the measured natural frequency and damping ratio of each beam for each configuration.

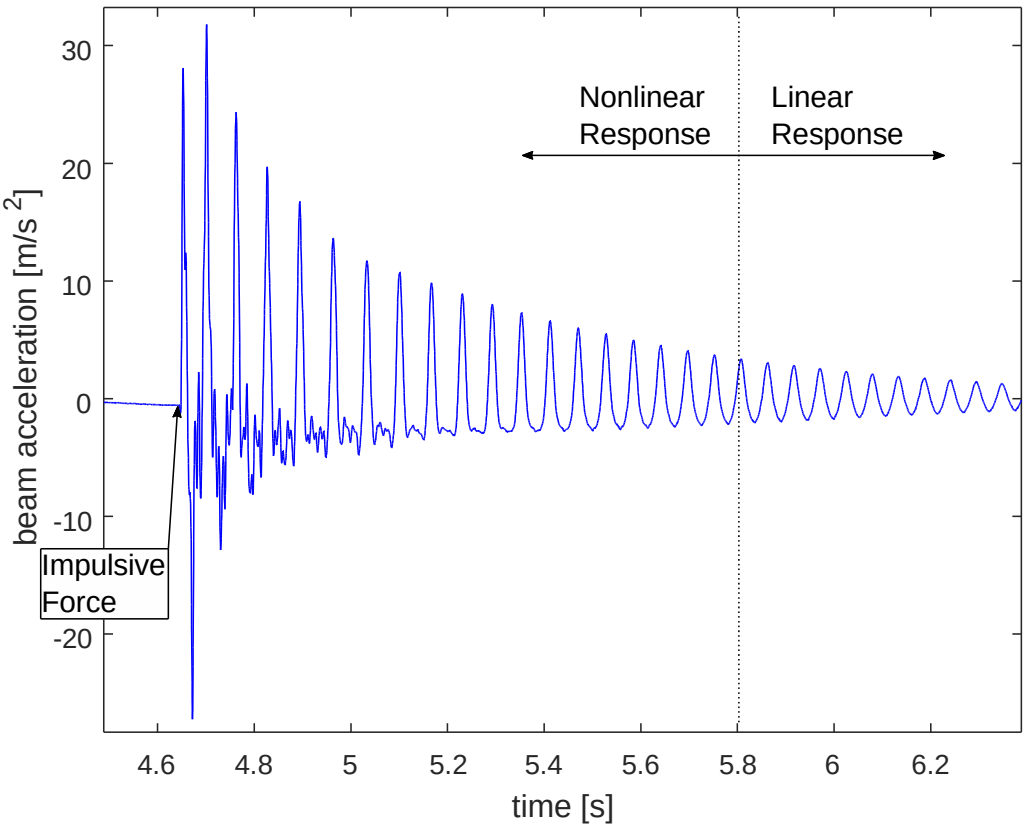

Figure 6. Example response from ring-down test. This test was conducted on beam 3, configuration 1.

Table 2: Natural frequency and damping ratio of each uncoupled beam considered.

configuration	Beam	Natural Frequency [Hz]	Damping Ratio [dim]
1	1	22.1	0.044
	2	16.6	0.034
	3	25.5	0.020
2	1	23.1	0.031
	2	21.3	0.032
	3	20.4	0.022
3	1	22.8	0.033
	2	13.7	0.059
	3	18.8	0.018

Once the linear natural frequencies and damping ratios for each beam have been determined, the parameters of each beam state are calculated by:

$$m_i = \frac{48\rho whL}{\pi^4} + 8m_{cube} + m_{acc} \tag{5}$$

$$b_i = 2\zeta\omega_n m_i \tag{6}$$

$$k_{L,i} = \frac{48EI}{L^3} \tag{7}$$

$$k_{NL,i} = \frac{2m_i\omega_n^{\,2}}{\Delta x_{eq}} \tag{8}$$

$$p_i = \frac{m_i\omega_n^{\,2}}{k_{L,i}} + 1 \tag{9}$$

In Equation 5, m_{cube} and m_{acc} are the mass of one square neodymium magnet (0.25 g) and the mass of the attached accelerometer (1 g), respectively, while w and h are the width (19.05 mm) and height (0.635 mm) of each spring steel beam. In Equation 8, Δx_{eq} is the measured distance between the stable equilibria of each bistable beam. The structural parameters given in Equations 5-9 are tabulated in Table 3 through Table 5 for all three configurations, respectively.

Table 3: Summary of structural parameters for configuration 1.

beam	m_i [g]	b_i [mN-s/m]	$k_{L,i}$ [N/m]	$k_{NL,i}$ [MN/m^3]	p_i [dim]
1	15.1	183	222	65	2.31
2	15.1	106	222	82	1.74
3	15.1	98	222	124	2.74

Table 4: Summary of structural parameters for configuration 2.

beam	m_i [g]	b_i [mN-s/m]	$k_{L,i}$ [N/m]	$k_{NL,i}$ [MN/m^3]	p_i [dim]
1	15.1	134	222	159	2.44
2	15.1	130	222	86	2.21
3	15.1	87	222	497	2.12

Table 5: Summary of structural parameters for configuration 3.

beam	m_i [g]	b_i [mN-s/m]	$k_{L,i}$ [N/m]	$k_{NL,i}$ [MN/m^3]	p_i [dim]
1	15.1	144	222	155	2.39
2	15.1	153	222	99	1.50
3	15.1	66	222	188	1.95

4 RESULTS AND DISCUSSIONS

4.1 Impedance trends in harmonic frequency sweeps

This research looks extensively at the experimentally measured impedance of a built-up multistable structure subjected to harmonic excitations. Here, results that are observed across all three configurations will be examined in detail. In all subsequent figures in this section that do not present time series of beam responses, the harmonic frequency sweep is shown in (a), while the real and imaginary components of impedance for beams 1, 2, and 3 are shown in (b), (c), and (d), respectively.

Figure 7 displays the response of configuration 3 subjected to a slow frequency sweep at 0.93 m/s^2. Even at this low amplitude, nonlinear dynamics are clearly present in beam 1, which undergoes a rapid change in response amplitude, termed a *bifurcation*, at approximately 13 Hz while increasing the excitation frequency, termed *frequency upsweep*, and 11.5 Hz while decreasing the excitation frequency, termed *frequency downsweep.* These bifurcations are marked in Figure 7(a) by black arrows beginning with a perpendicular bar on the frequency upsweep and with a solid dot on the frequency downsweep. During these rapid transitions between low- and high-amplitude responses, the reactance of beam 1 is observed to rapidly transition between positive and negative values, shown in Figure 7(b) by arrows corresponding with those in Figure 7(a). This indicates that dynamic bifurcations of multistable system components exhibit quickly vanishing drive-point reactance when subjected to low amplitude harmonic frequency sweeps. Since reactance corresponds to the effectiveness of reciprocal energy exchange among system components, it is hypothesized that this bifurcation occurs due to the inability of beam 1 to effectively transfer energy to other components and cannot dissipate excess energy via damping mechanisms, and must therefore transition into a dynamic regime characterized by a larger amplitude response.

The nonlinear dynamics of beams 2 and 3 occur between 16 Hz and 24 Hz, where two nonlinear resonances occur, marked by four- and five-pointed stars in Figure 7(a). The corresponding stars in Figure 7(c,d) indicate that a gradual crossing across zero reactance occurs in the transfer impedance of multistable structures when they pass through a nonlinear resonance when subjected to low amplitude harmonic excitation. Since reactance corresponds to the effectiveness of energy reciprocity among system components, it is hypothesized that during resonance, the beams lose the ability to effectively transfer energy to other components but can dissipate excess energy via damping mechanisms and thus do not transition into a different dynamic regime. In fact, it is observed that the amplitude response of beam 3 at the first identified resonance (five-pointed star) is greater than that measured for beam 2 at the same frequency as well as that measured for both beams 2 and 3 at the second identified resonance (four-pointed star). This may be due to the fact that the resistance of beam 3 at the first resonance is close to zero in comparison to these other measurements, which indicates a reduced ability to dissipate energy and therefore results in a larger amplitude response.

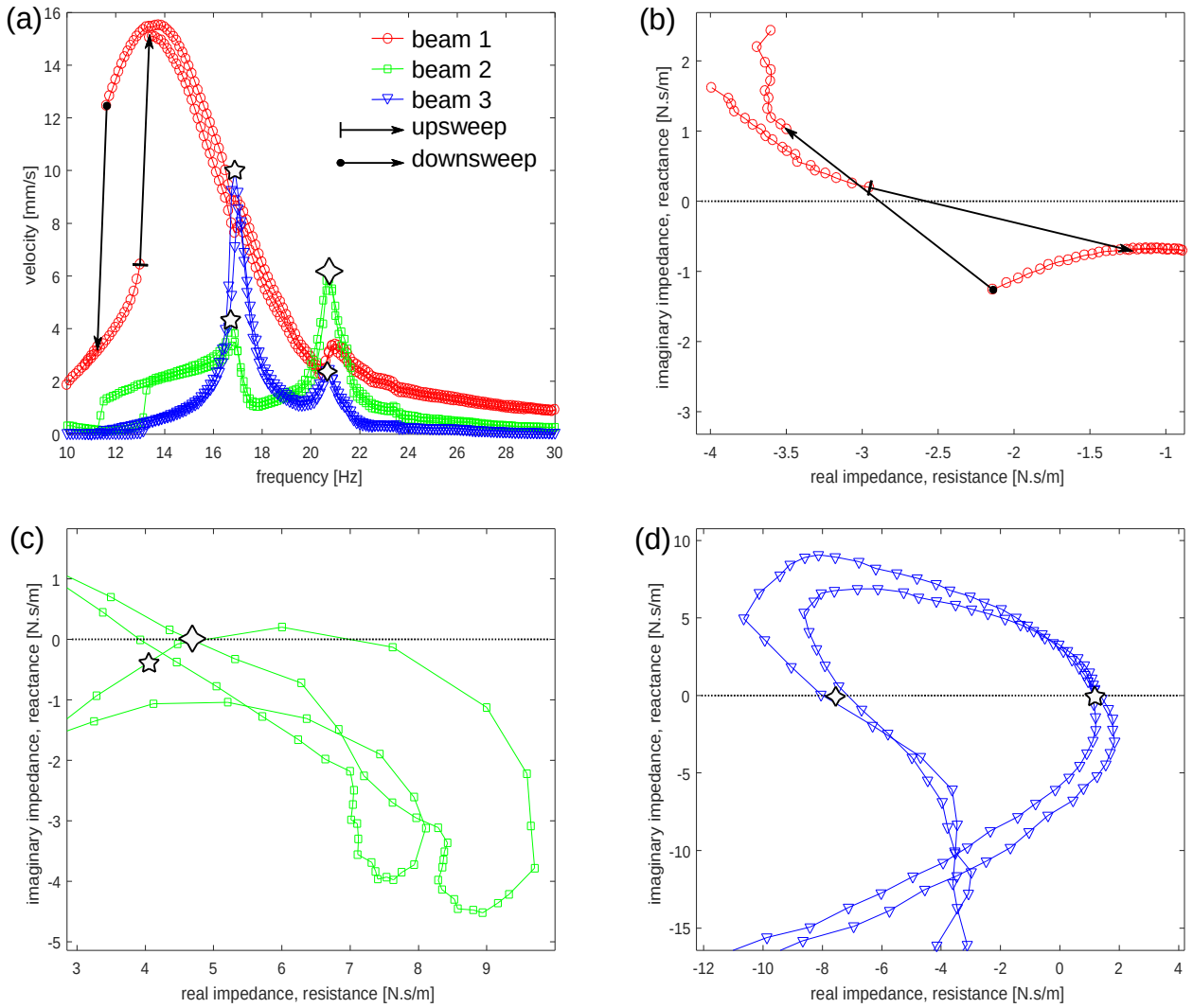

Figure 7. Frequency sweep conducted on configuration 3 with A=0.93 m/s^2. (a) frequency response of all three beams; (b) beam 1 impedance; (c) beam 2 impedance; (d) beam 3 impedance.

Figure 8 compares the beam accelerations before and after the identified bifurcation of beam 1 during the frequency upsweep, noted in Figure 7(a) by the solid black arrow at approximately 13 Hz. While higher order harmonics are exhibited, a significant increase in amplitude is observed to occur due to an inability to effectively transfer the input energy to other system components. The upsweep bifurcation of beam 1 in Figure 7(a) also causes the amplitude of beam 2 to increase, and provides enough excitation force to overcome the stick-slip friction present in beam 3's bearings which allows the beam to begin responding, also seen in Figure 7(a) at approximately 13 Hz. All beams are observed to oscillate with the same relative phase and manifest harmonics before and after the bifurcation, indicating that only the relative amplitudes of the dynamic responses changed during this dynamic regime change.

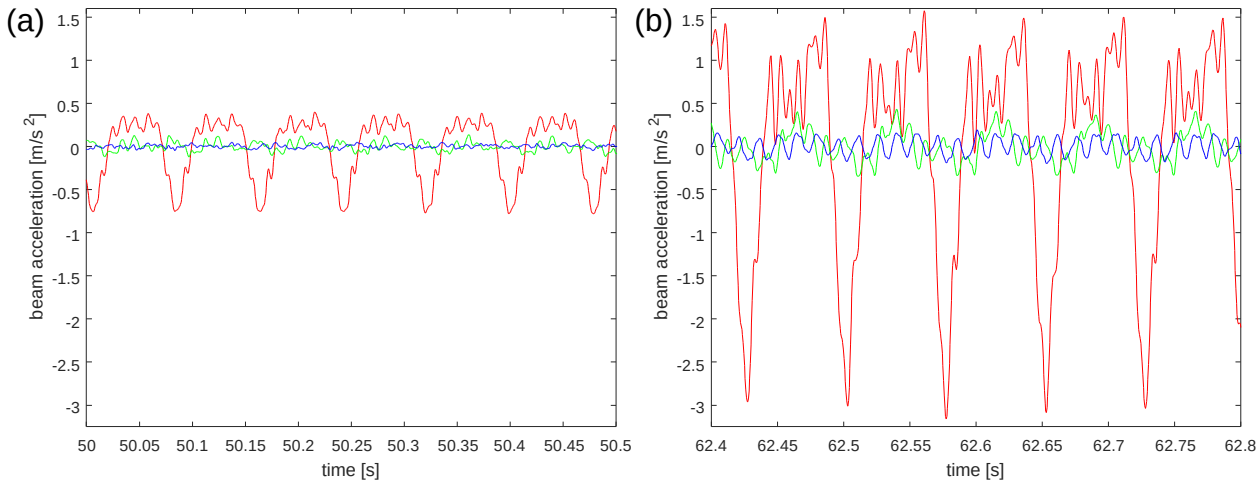

Figure 8. Time domain response of configuration 3 beam accelerations as measured experimentally (a) before beam 1 bifurcation; (b) after beam 1 bifurcation. Input acceleration A=0.93 m/s^2.

Figure 9 displays the response of configuration 1 when subjected to a harmonic frequency sweep with a constant amplitude of 2.85 m/s^2. At this amplitude, clear bifurcations occur for all three beams, denoted by the solid black arrows in Figure 9(a). Unlike the lower amplitude case in Figure 7, the reactance of beam 1 does not change sign through this dynamic regime change. Rather, reactance jumped to a small, but still negative, value shown in Figure 9(b) by solid black arrows corresponding with those in Figure 9(a). Yet, this is still indicative of reactance rapidly approaching zero at the onset of a naturally sudden change in dynamic response and denotes a loss in the ability of beam 1 to effectively transfer excess energy to other system components.

Beams 2 and 3 exhibit dynamic bifurcations when passing through nonlinear resonances, denoted by the solid black arrows in the green and purple shaded regions of Figure 9(a). These bifurcations correspond with rapid transitions across zero reactance in both transfer impedance plots of Figure 9(c,d), where the solid black arrows in green and purple shaded regions correspond to those in Figure 9(a). These sudden transitions to higher-amplitude dynamic regimes (and corresponding rapidly vanishing reactance), which may correspond with up to almost a tripling of the response amplitude in about 5 seconds, which is the amount of time each data point in Figure 9 is averaged over, contrast with the gradual transitions observed in Figure 7(a), which exhibits closely spaced data points throughout the non-bifurcating resonances, a discrepancy likely due to the increased energy input into the system that each DOF must manage. Rather than gradually transitioning into higher amplitude responses, beams 2 and 3 must instead transition into higher amplitude dynamic regimes suddenly in order to manage effectively manage the input energy. It is noted that the change from low to large amplitude response of beam 2 during the nonlinear resonance at approximately 23 Hz, denoted by the purple shaded region in Figure 9(a), is not as rapidly changing as that exhibited by beam 3 at the same frequency. However, it is noted that the impedance measured for beam 2 exhibits zero reactance just before the large amplitude resonance occurs, denoted by corresponding pentagons in Figure 9(a,c), which predicts a loss in effective energy exchange among the beams and leads to the large amplitude resonant response seen in Figure 9(a).

It is also observed that local minima in the frequency response of each beam manifest as curved arcs, which loop back around on themselves unless interrupted by a sudden bifurcation, as in the case with beam 1. In the case of beam 2, this minima loop also corresponds with a crossing of zero reactance in between nonlinear resonances, denoted by circles in Figure 9(a,c), which is a conventional trend in impedance change typically seen in systems with multiple DOF when passing through an antiresonance.

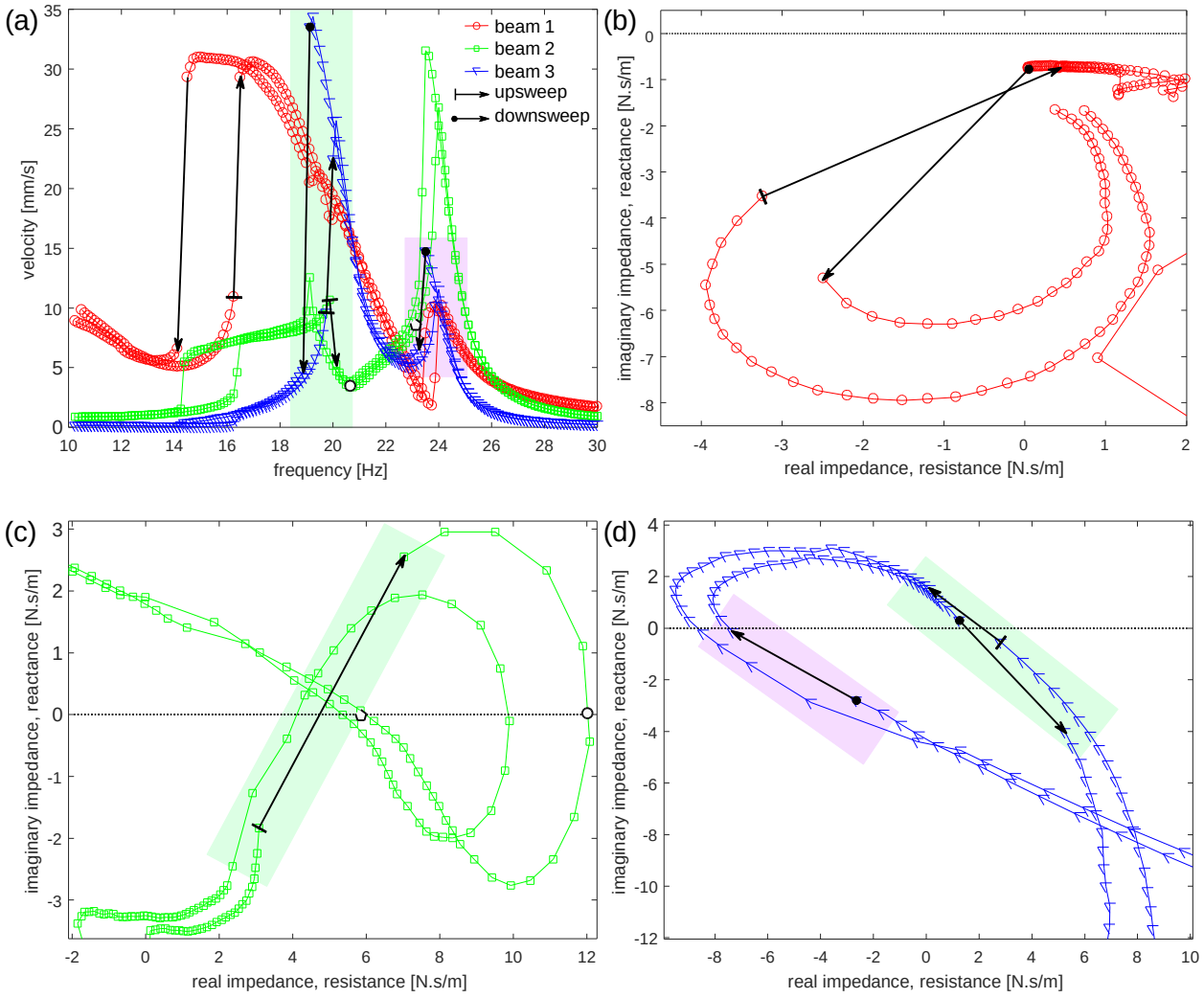

Figure 9. Frequency sweep conducted on configuration 3 with A=2.85 m/s^2. (a) frequency response of all three beams; (b) beam 1 impedance; (c) beam 2 impedance; (d) beam 3 impedance.

Figure 10 compares the beam acceleration response in the time domain before and after the bifurcations and nonlinear dynamics noted in Figure 9(a). Figure 10(a,b) denotes the response just before and after the bifurcation of beam 1 observed in Figure 9(a) on the frequency upsweep at approximately 16 Hz. It is seen that this bifurcation greatly increases the response amplitudes of beams 1 and 2, while all beams remain in-phase both pre- and post- bifurcation. By contrast, the time-domain response before and after the upsweep bifurcation denoted by the green region in Figure 9(a) is shown in Figure 10(c,d). This bifurcation alters the response amplitude of beam 3 by a significant degree, but results in all three beams oscillating 90° out

of phase with one another, each beam lagging previous beam in the sequence, which indicates a resistance to the instantaneous transfer of energy between beams and therefore larger response amplitudes. The time-domain response of each beam after and before the bifurcation that occurs at the resonance denoted by the purple region of Figure 9(a) on the frequency downsweep is shown in Figure 10(e,f). Figure 10(f) shows the high-amplitude response just before the bifurcation on the frequency downsweep, while Figure 10(e) displays the low-amplitude response just after this bifurcation occurs. This nonlinear resonance leads to a decreased response amplitude of all three beams and leads to beam 1 and 2 moving in phase with each other in the low amplitude response, Figure 10(e), rather than beam 2 lagging beam 1 by about 90°, Figure 10(f). Both before and after this bifurcation, beams 2 and 3 oscillate perfectly out of phase.

The responses shown in Figure 10 also indicate that higher-order harmonics tend to manifest in this experimental system at lower excitation frequencies. As the excitation frequency increases, such as by viewing Figure 10(a) to (c) to (e), the higher-order harmonics tend to disappear until the response of all three beams nearly manifests only the fundamental frequency which matches the excitation frequency, a response trend particularly observed in the data of Figure 10(f). This occurs since the system is being excited close to fundamental natural frequencies, so the dynamic response mostly manifests as a single mode shape. These higher-order harmonics manifest at low frequencies no matter the excitation frequency sweep direction.

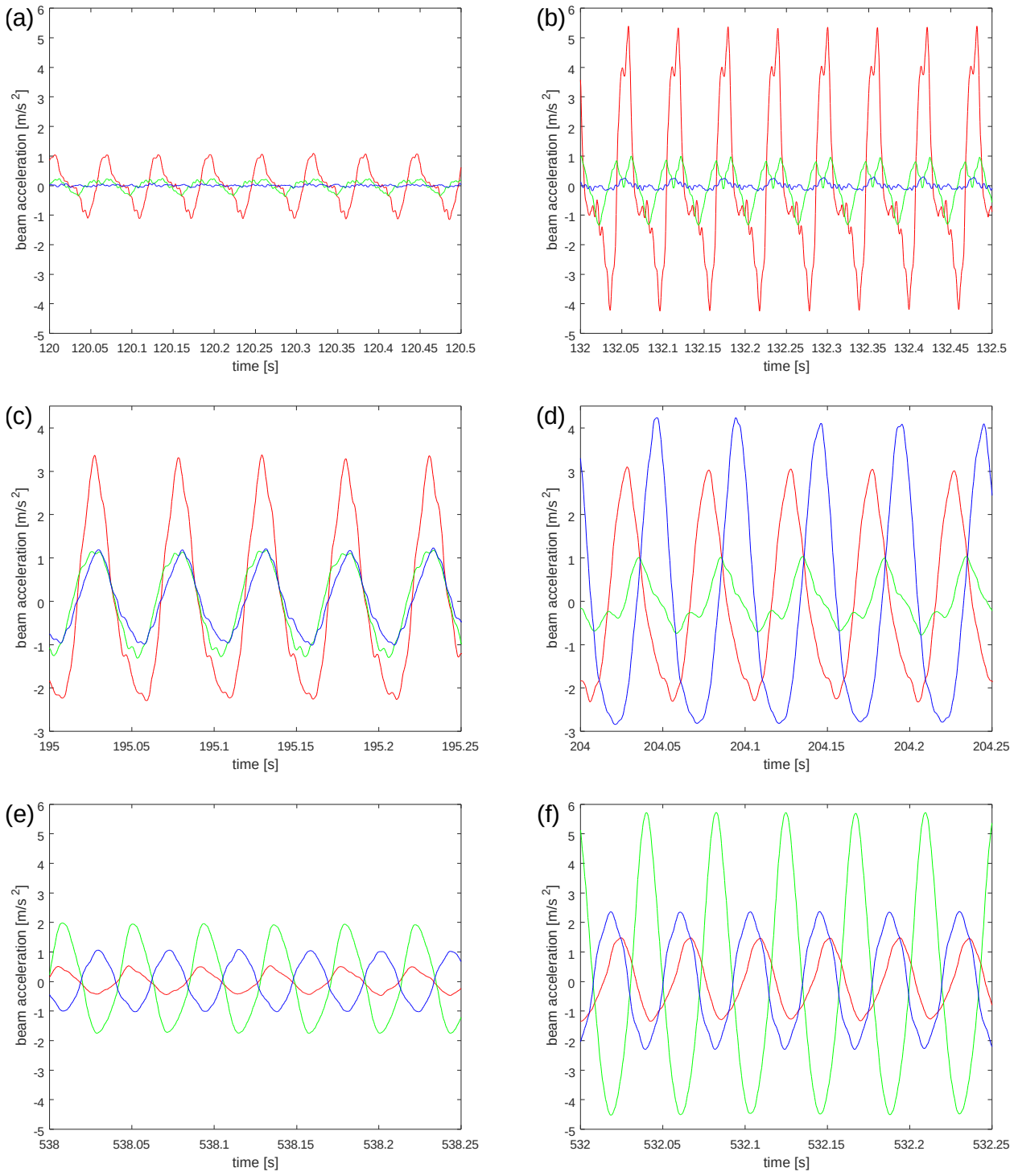

Figure 10. Time domain response of configuration 1 beam accelerations as measured experimentally (a) before bifurcation at 16 Hz on excitation frequency upsweep; (b) after bifurcation at 16 Hz on excitation frequency upsweep; (c) before green region bifurcation at 20 Hz on excitation frequency upsweep; (d) after green region bifurcation at 20 Hz on excitation frequency upsweep; (e) after purple region bifurcation at 24 Hz on excitation frequency downsweep; (f) before purple region bifurcation at 24 Hz on excitation frequency downsweep. Input acceleration A=0.93 m/s^2.

A representative example of a high excitation amplitude frequency sweep response is shown in Figure 11, which displays the frequency and impedance responses of configuration 2 due to a constant 6.63 m/s^2 input from the electrodynamic shaker. Note that only results from periodic steady-states are shown in Figure 11, since a region of aperiodic response in the 14 Hz to 17 Hz frequency range is prevalent, particularly in the response from beam 1.

At this high excitation amplitude, snap-through is observed to occur for all three beams at low frequencies, as seen by the highest velocities presented in Figure 11(a), which are more than four times greater than the highest velocities of Figure 7(a) and Figure 9(a). The characterization of the transition between high-amplitude snap-through and other low-amplitude responses is of critical importance to the design of complex, multistable structures since this transition is a primary mechanism by which the structural integrity of the system may be compromised. This transition is denoted by the dashed arrows in Figure 11(a), with perpendicular bars indicating the start of the transition on the frequency upsweep and filled circles indicating the start of the transition on the frequency downsweep. Corresponding dashed arrows are also shown on the drive-point and transfer impedance plots in Figure 11(b,c,d), which indicate that a transition between snap-through and low amplitude responses during harmonic frequency sweeps is accompanied by a corresponding, sudden change in impedance that crosses through zero reactance for all three beams. As with the low amplitude harmonic frequency cases, the observed transition between snap-through and low amplitude intrawell responses represents a bifurcation between low and large amplitude steady-states, and corresponds to sudden transitions across zero reactance. This represents a sudden loss in the ability of each beam to effectively transfer energy to other system components and must therefore transition into another steady-state due to a loss in the dynamic stability of the snap-through state.

In addition, a second set of bifurcations are observed to occur around 19 Hz, denoted by the solid arrows in the frequency response plot, Figure 11(a), and corresponding arrows in the impedance plots in Figure 11(b,c,d). This set of bifurcations also corresponds to both vanishing drive-point and transfer impedances. If one considers dynamic bifurcations as a severe case of nonlinear resonance, these results indicate that no matter the excitation amplitude level, multistable structures subjected to harmonic frequency sweeps exhibit vanishing drive-point and transfer reactance when crossing through nonlinear resonances on both frequency upsweeps and downsweeps. This trend for transitions from low to high amplitude and vice versa. Therefore, it is hypothesized that nonlinear resonances and dynamic bifurcations occur when a structural component temporarily loses an energy management mechanism, in this case reciprocal energy exchange between DOF when subjected to harmonic excitation frequency sweeps.

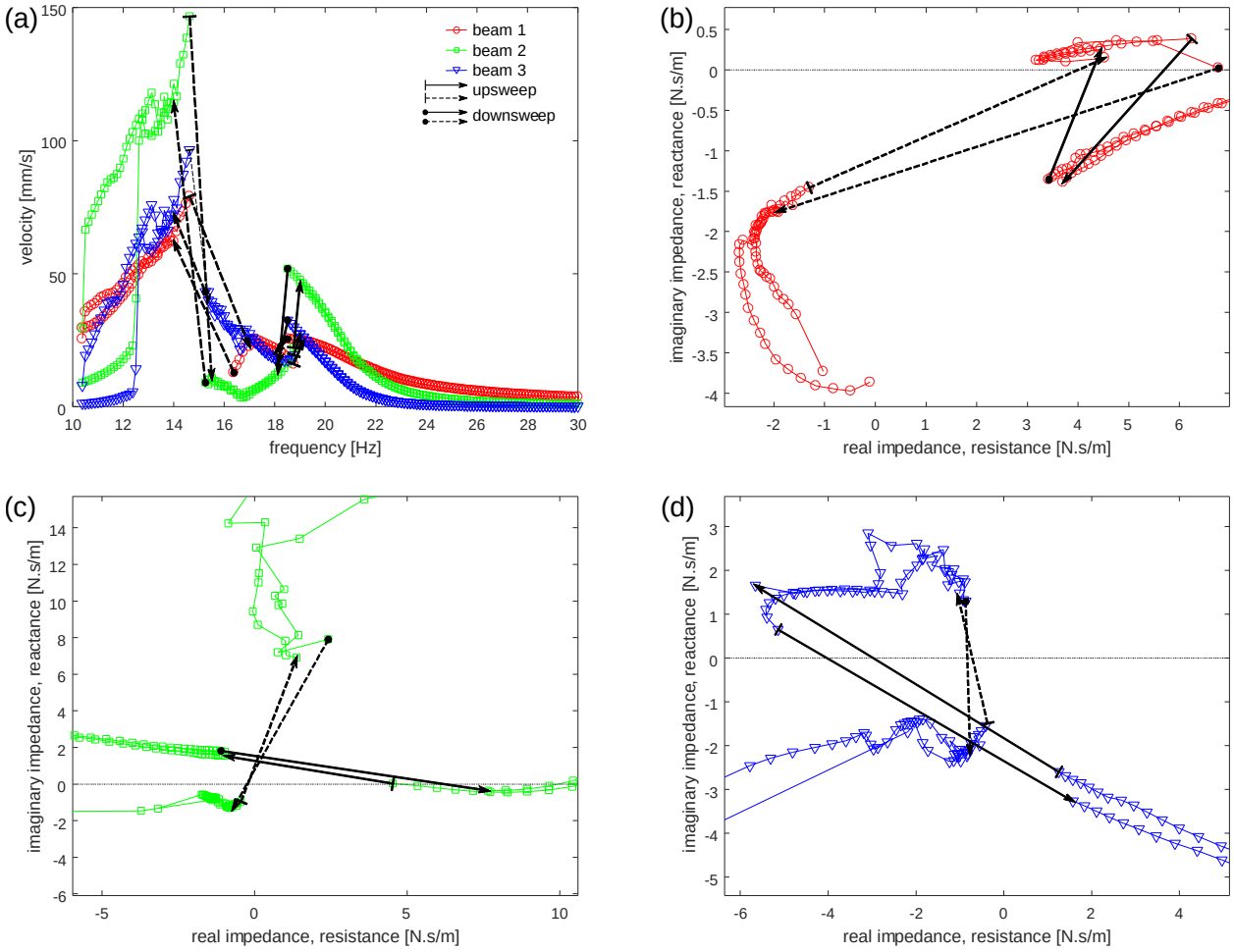

Figure 11. Frequency sweep conducted on configuration 2 with A=6.63 m/s^2. Only periodic steady-states are shown. (a) frequency response of all three beams; (b) beam 1 impedance; (c) beam 2 impedance; (d) beam 3 impedance.

Figure 12 compares the snap-through dynamic response with the small-amplitude steady-state that it transitions into. During the interwell dynamic shown in Figure 12(a), all three beams snap through with slight phase lags between adjacent beams, indicating a system-level interwell response, although higher-order harmonics are present. By contrast, the periodic steady-state it transitions into, seen in Figure 12(b), results in beam 2 almost completely unresponsive while beams 1 and 3 oscillate 180˚ out of phase, which corresponds to one of the mode shapes of a linear, 3DOF system [24]. The higher-order harmonics that are present in the snap-through response but not in the low amplitude interwell response are likely a result of the quasi-linear nature of low-amplitude responses in multistable systems, which approximates a collection of coupled simple, harmonic oscillators.

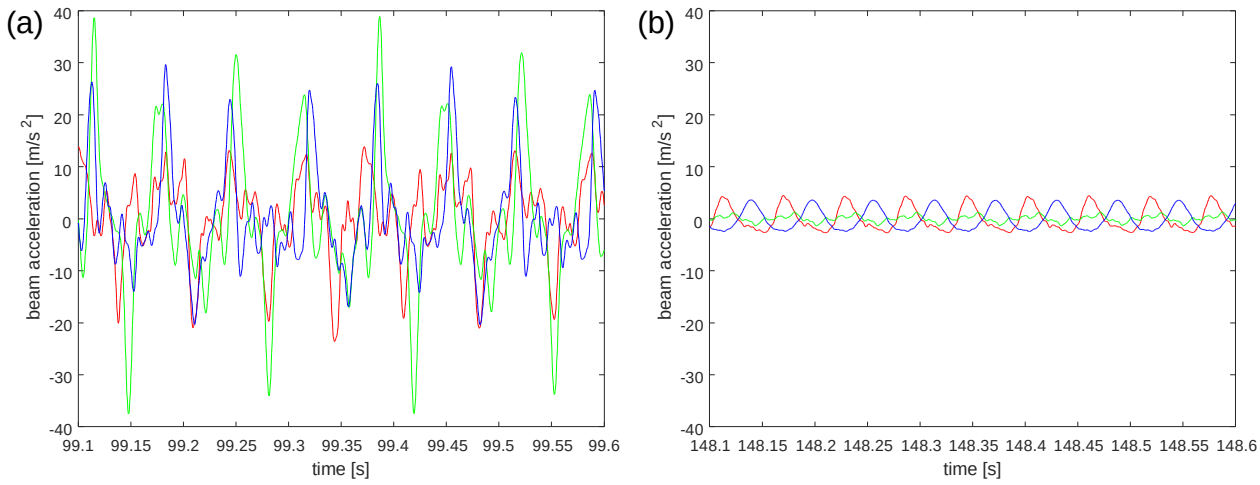

Figure 12. Time domain response of configuration 2 beam accelerations as measured experimentally (a) during snap-through response; (b) during low-amplitude intrawell response. Input acceleration A=6.63 m/s^2.

4.2 Impedance trends in amplitude sweeps

In this section, typical results of harmonic amplitude sweeps conducted at constant frequency are examined in detail. In all subsequent figures in this section that do not showcase time series of beam responses, the harmonic amplitude sweep is shown in the respective figure part (a), while the impedance of beams 1, 2, and 3 are shown in parts (b), (c), and (d), respectively.

Figure 13 displays the response of configuration 2 subjected to a slow excitation amplitude sweep conducted at 11 Hz, chosen due to the observed coexistent dynamic responses at this frequency. One bifurcation is observed to occur for beams 1 and 2 on both the amplitude upsweep and amplitude downsweep, denoted by the solid black arrows in Figure 13(a), while beam 3 remains relatively unresponsive throughout the entirety of the experiment. Due to this relative lack of activity, the impedance plot of beam 3 in Figure 13 is excluded in order to focus on the more interesting dynamics of the other two beams. The results for beam 2 for this case are much the same as they were with regards to frequency sweeps: the bifurcations noted in Figure 13(a), which transition from low to high response amplitude in approximately 5 seconds, cause the reactance of that beam to vanish correspondingly quickly in the midst of this transition, shown in Figure 13(c) by solid black arrows which correspond to those in Figure 13(a). Interestingly, the impedance of beam 1 crosses over the zero resistance line during these bifurcations, marked in Figure 13(b) by solid black arrows corresponding to those in Figure 13(a), rather than the zero reactance line, in contrast to the results obtained from the frequency sweeps. This indicates that the bifurcation seen in the response of beam 1 is the result of a sudden loss in the ability of beam 1 to effectively transfer away or otherwise dissipate excess energy, which necessitates a rapid increase in response amplitude in order to effectively manage the increasing amount of input energy.

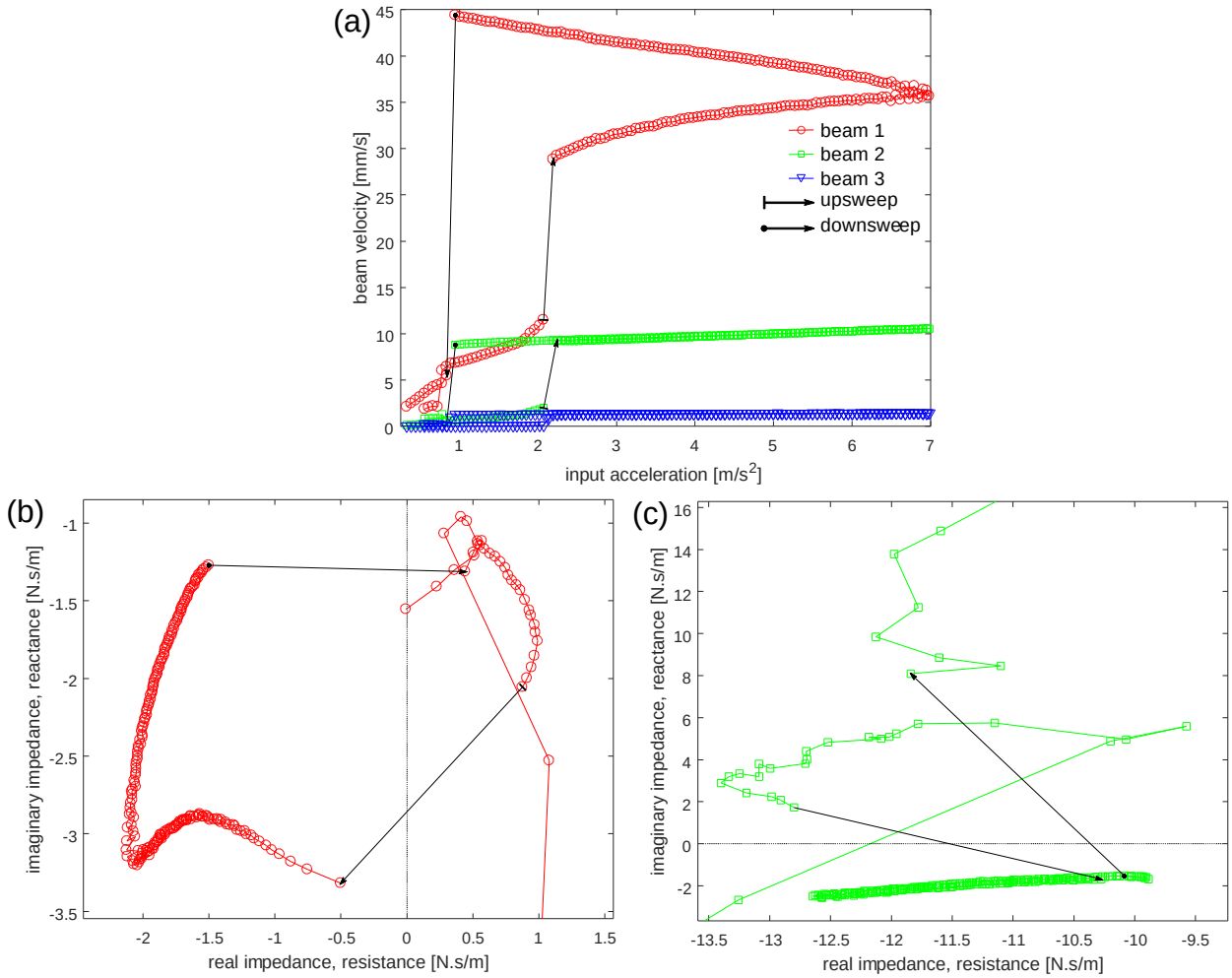

Figure 13. Amplitude sweep conducted on configuration 2 with f=11 Hz. (a) amplitude response of all three beams; (b) beam 1 impedance; (c) beam 2 impedance.

Figure 14 shows how the dynamics of this system change due to the bifurcation that occurs on the excitation amplitude upsweep at approximately 2 m/s^2 in Figure 13(a), and displays the low amplitude response, Figure 14(a), before it transitions into a high-amplitude regime, Figure 14(b). The high-amplitude response is characterized by beam 1 snapping through while the other two beams oscillate at lower amplitudes but in phase with beam 1. By contrast, the low amplitude response is characterized by beams 2 and 3 oscillating out of phase from one another, while the second harmonic of beam 1 is dominant, which results in a response frequency that is half of the excitation frequency. This multi-harmonic response is observed by the slow frequency modulation of the instantaneous acceleration of beam 1 in Figure 14(a).

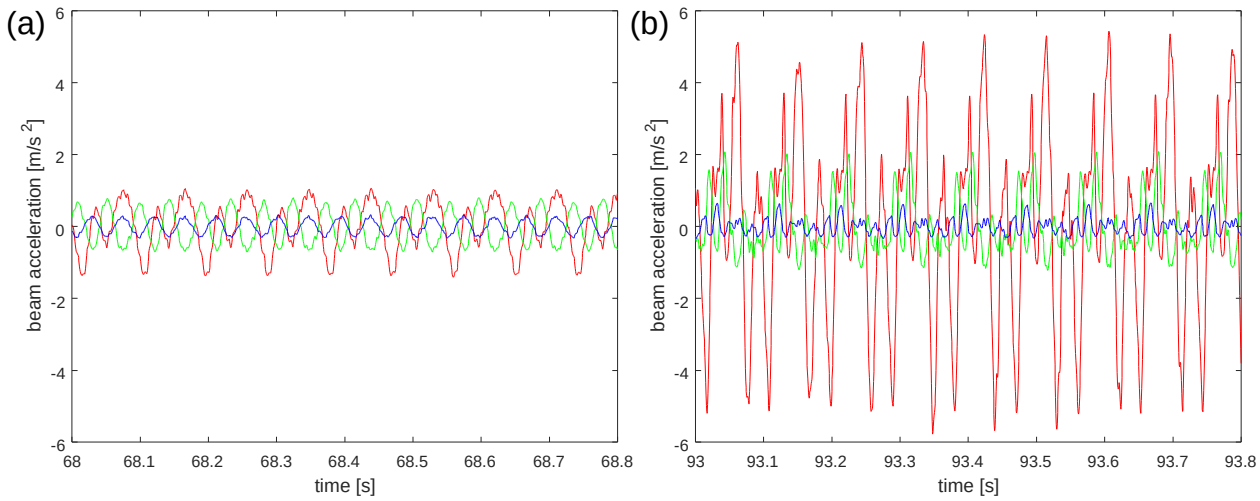

Figure 14. Time domain response of configuration 2 beam accelerations as measured experimentally (a) before bifurcation; (b) after bifurcation. Excitation frequency f=11 Hz.

Figure 15 shows the response of configuration 2 subjected to an amplitude sweep with an excitation frequency of 16 Hz, chosen because of the observed coexistent dynamic responses occurring at this frequency, and its nearness to observed nonlinear resonances. As the excitation amplitude increases, all three beams suddenly transition into a sustained region of aperiodic response, denoted by the yellow shaded regions of Figure 15. While this aperiodic response appears to be manifest as a drop in beam velocity in Figure 15(a) in comparison to the higher-amplitude, periodic responses of each beam, this conclusion is misleading. Examining the acceleration time series in Figure 16 before (a), during (c), and after (e) the aperiodic dynamic regime, one notes that the maximum amplitude of the aperiodic response is up to three times greater than that of either of the other steady-state responses. This decreased response amplitude in the frequency domain is due to the random variation in response amplitude present during aperiodic dynamics averaged over time. In reality, however, this dynamic regime is problematic for built-up structures. Since fatigue life is governed in part by the peak-to-peak stress amplitude [25], this aperiodic response can decrease the fatigue life of a structural component in comparison to that predicted by its constant amplitude steady-states, even though Figure 15(a) appears to indicate the opposite. The same aperiodic characteristics are observed to occur on the amplitude downsweep between from 2.6 m/s^2 and 3.3 m/s^2, denoted in Figure 15 by the blue shaded region. While this region appears more consistent than the first region of aperiodic response, an examination of the time series in Figure 16 before (b), during (d), and after (f) this region qualitatively indicates a consistent shape with varying amplitude, which changes by up to a factor of three in this region, inducing the same issues with fatigue life as the first aperiodic regime.

Figure 15 also indicates several noteworthy trends. Aside from the transition into aperiodic regimes, beam 1 exhibits no dynamic bifurcations or other interesting dynamic trends. However, the plots of transfer impedance for beams 2 and 3, shown in Figure 15(c,d) respectively, both indicate that the onset of a large amplitude, aperiodic response is associated with a sudden transition across zero transfer reactance. In addition, beam 3 undergoes a dynamic bifurcation on the amplitude downsweep at approximately 1.5 m/s^2, marked by a solid black arrow in Figure 15(a), which corresponds to another rapid transition across zero

reactance in Figure 15(d). These results not only reinforce observed impedance trends regarding dynamic bifurcations between steady-states, but also indicate that the onset of aperiodicity may be predicted by a vanishing transfer reactance. Still, aperiodicity has long been acknowledged to be a significant hindrance to the study of multistable structures [6] [16], and more investigation into this phenomenon is necessary in order to understand what makes a structure more susceptible to its manifestation.

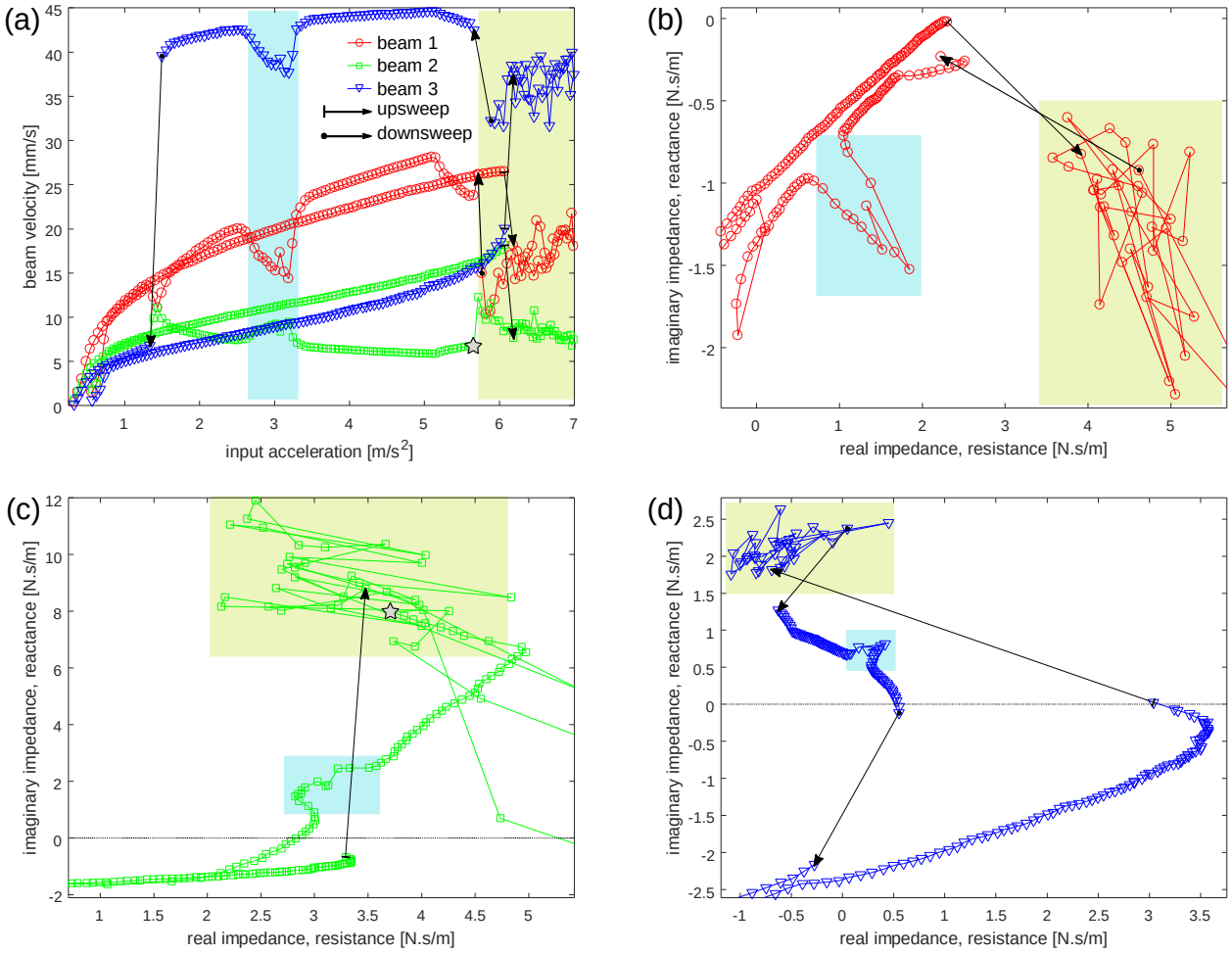

Figure 15. Amplitude sweep conducted on configuration 3 with f=16 Hz. Clear regions of aperiodic behavior are visible, denoted by the yellow and blue shaded areas. (a) amplitude response of all three beams; (b) beam 1 impedance; (c) beam 2 impedance; (d) beam 3 impedance.

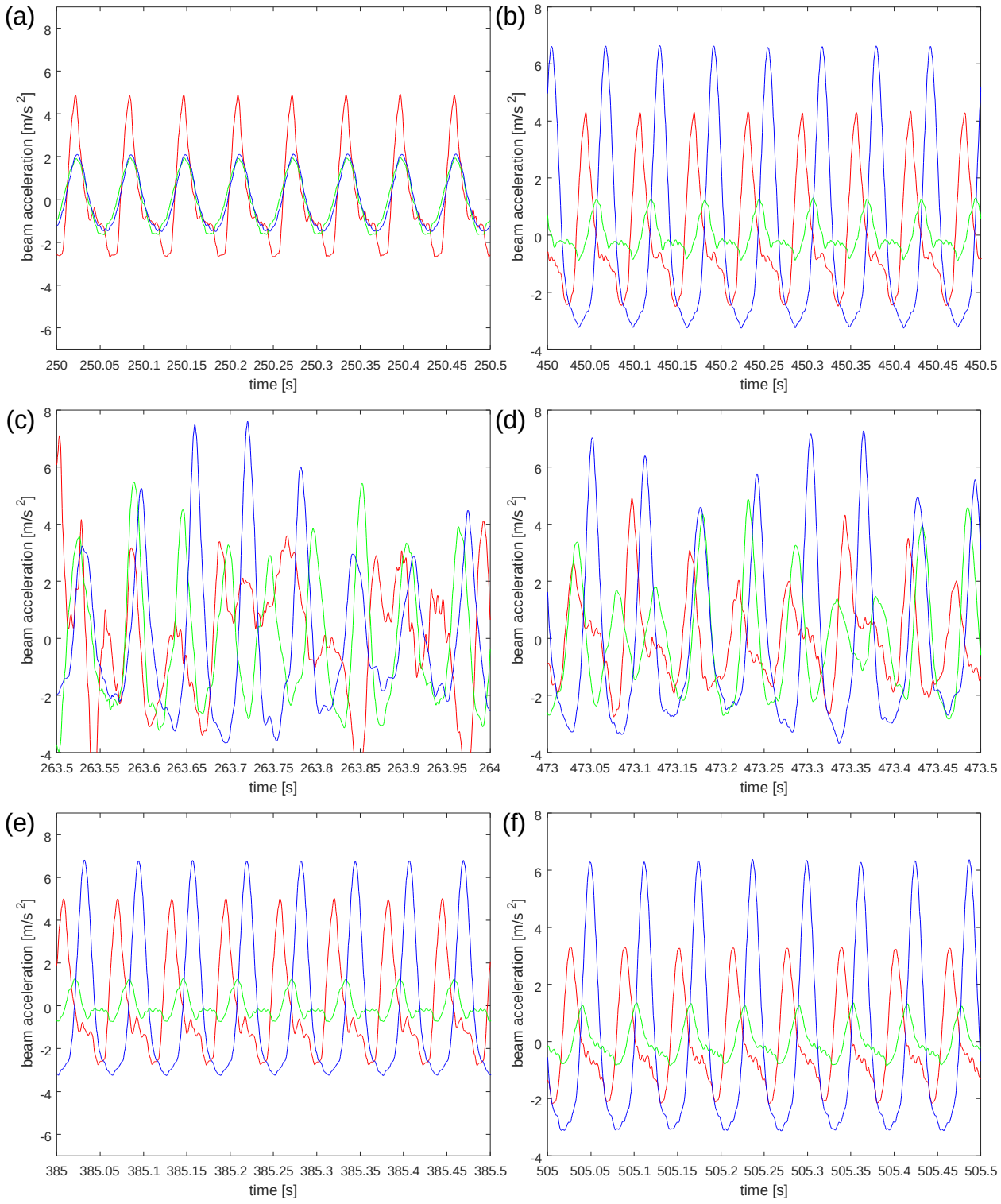

Figure 16. Time domain response of configuration 2 beam accelerations as measured experimentally (a) before first (yellow) aperiodic regime (b) before second (blue) aperiodic regime; (c) during first (yellow) aperiodic regime; (d) during second (blue) aperiodic regime; (e) after first (yellow) aperiodic regime; (f) after second (blue) aperiodic regime. Excitation frequency f=16 Hz.

Figure 17 shows the results of an amplitude sweep conducted on configuration 3 at an excitation frequency of 17 Hz, chosen due to the coexistent dynamic responses observed during the harmonic frequency sweep experiments. A bifurcation is seen to occur for beams 1 and 3 between 1 m/s^2 and 1.5 m/s^2 on both the amplitude upsweep and amplitude downsweep, while this only occurs on beam 2 for the upsweep, all of which are marked by solid black arrows in Figure 17(a). The impedance trends of this experiment tracked well with the previously discussed results. The bifurcations observed in the response of beam 1 again nearly correlate with a vanishing resistance rather than a vanishing impedance as seen via the arrows in Figure 17(b) that correspond with those in the amplitude response plot of Figure 17(a), while the reactance of both beams 2 and 3 are observed to vanish soon after the large change in system dynamic response occurs, marked in Figure 17(c,d) with solid black arrows corresponding to those in Figure 17(a). These results indicate that dynamic bifurcations in multistable structures subjected to constant frequency harmonic amplitude sweeps correspond to vanishing resistance in drive-point impedance measures and vanishing reactance in transfer impedance measures. For drive-point measurements, this may be due to the inability of the first structural component to dissipate the increasing amount of input energy via damping mechanisms. For transfer measurements, this may be due to the inability of subsequent structural components to effectively manage energy via exchange with other components, which, coupled with a potential inability of some system components to dissipate energy, may lead to transfer components transitioning into new dynamic regimes to accommodate an increasing energy input into the system.

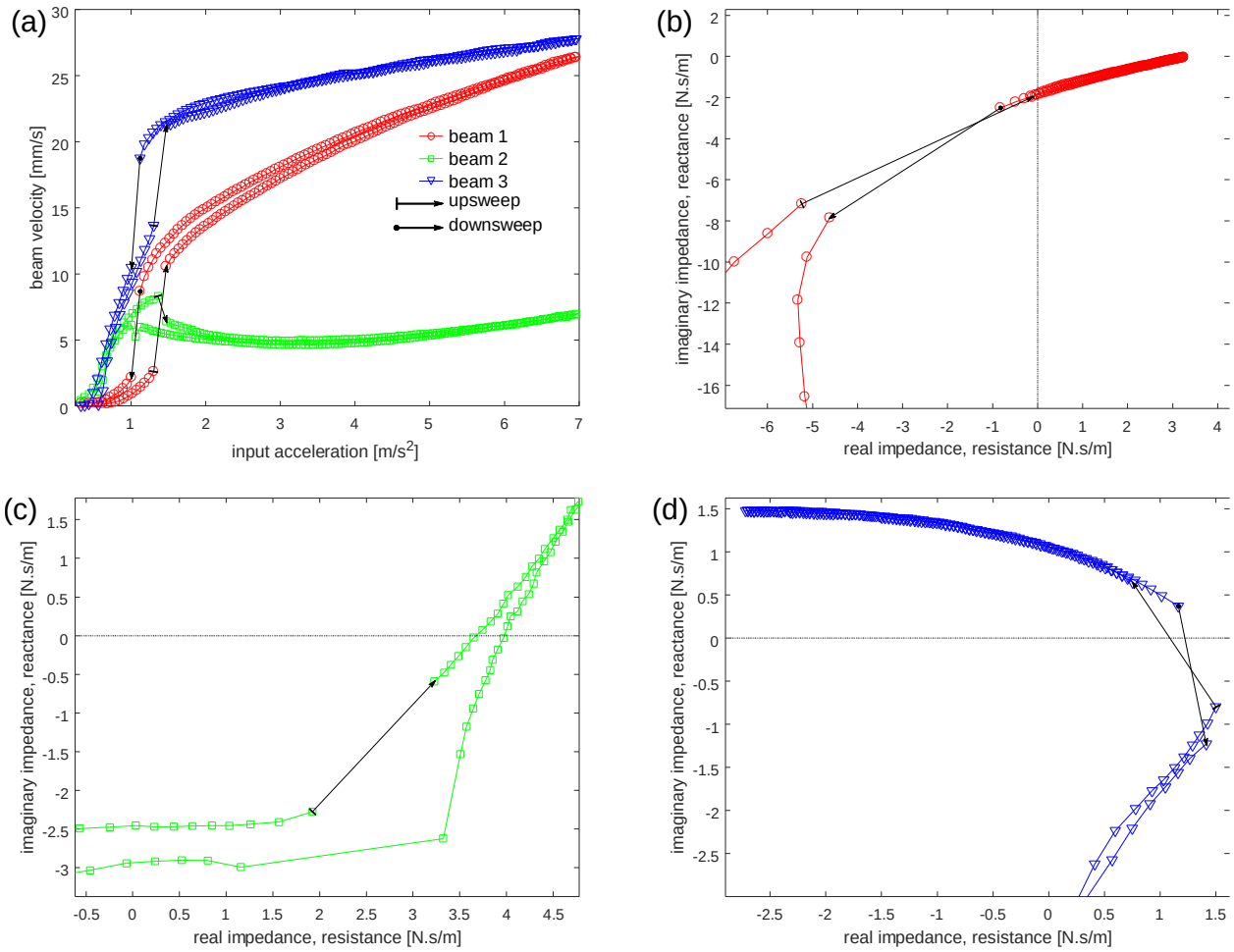

Figure 17. Amplitude sweep conducted on configuration 3 with f=17 Hz. (a) amplitude response of all three beams; (b) beam 1 impedance; (c) beam 2 impedance; (d) beam 3 impedance.

4.3 Summary of results

The experimental evidence obtained through this research indicates that mechanical impedance measurements of multistable structures subjected to harmonic excitations exhibit several interesting trends, depending on the excitation feature that is varied and whether the impedance measurement is drive-point or transfer. For harmonic excitation frequency sweeps at constant excitation amplitude, it is found that dynamic bifurcations and nonlinear resonances correspond to vanishing reactance, no matter whether the measurement is of drive-point or transfer impedance. For harmonic excitation amplitude sweeps at constant excitation frequency, it is found that dynamic bifurcations again correspond to vanishing reactance if the measurement is of transfer impedance. In contrast to harmonic excitation frequency sweeps, it is found that the drive-point resistance of multistable structures vanishes at dynamic bifurcations during harmonic excitation amplitude sweeps. These vanishing reactance or resistance values represent a temporary loss in a particular form of energy management mechanism, either reciprocal energy exchange among DOF, in the case of reactance, or energy transfer and damping mechanisms in the case of resistance. These results are summarized in Table 6.

Table 6. Summary of drive-point and transfer impedance trends observed during harmonic excitation frequency and excitation amplitude sweeps.

Test Type	Input Harmonic Amplitude	Input Harmonic Frequency	Drive-Point Impedance Trend at Bifurcation	Transfer Impedance Trend at Bifurcation
Harmonic Frequency Sweep	Nonzero constant	Slow sweep 10-30 Hz	Vanishing reactance	Vanishing reactance
Harmonic Amplitude Sweep	Slow sweep 0.25-7 m/s^2	Nonzero constant	Vanishing resistance	Vanishing reactance

5 CONCLUSION

Multistability is a structural property that manifests in a wide range of applications. It can be used to enhance the performance of energy harvesters, or make slender structural components undergo large amplitude dynamics. In the context of skin buckling, this can lead to structural damage due to fatigue and decreased flight performance characteristics due to uneven surfaces, but may also relieve thermal stress by expanding into a multistable configuration. The difficulty in implementing such a multistable structure in a real world application lies in a lack of understanding on how the dynamics of one local instance of multistability can influence neighboring dynamics, and how to predict undesirable dynamic behaviors in complicated, built-up structures.

Utilizing an archetypal multistable structure that represents a complex, built-up system such as a buckled, rib-stiffened panel, this research experimentally investigates one potential avenue for predicting the dynamic response of these complex structures in real time. By measuring the dynamic response at various points on a structure, and the input force at a single point, one can measure the impedance of this structure in real time at various locations, which can serve as a warning regarding when significant changes in dynamic response are about to occur.

The experimental platform for this investigation is designed to be representative of a system of post-buckled aircraft panels while significantly reducing the complexity of the system. It is found that under constant-frequency harmonic frequency sweeps, both drive point and transfer impedance measurements indicate that reactance, the imaginary component of impedance, vanishes when nonlinear resonance and bifurcations occur. The former corresponds to a gradual crossing from negative to positive impedance (or vice versa), while the latter is characterized by a sudden jump across the line of zero impedance. It is hypothesized that this is due to a loss in dynamic stability of the structure's current steady-state due to structural components exhibiting an inability to transfer energy among one another and can therefore no longer manage all the input energy via solely damping mechanisms.

It is also found that under constant-frequency harmonic amplitude sweeps, the same trend occurs in transfer impedance measurements; the reactance vanishes when bifurcations occur between periodic steady-states, which are characterized by sudden jumps across the zero impedance line. However, the drive point impedance measurements under these amplitude sweeps indicate that resistance, the real component of impedance, vanishes when a bifurcation occurs. It is hypothesized that this loss in dynamic stability is due to a combination of drive-point structural components losing the ability to manage increasing total energy via damping mechanisms coupled with transfer structural components losing the ability to transfer energy among one another.

Thus, these experimental results provide the basis for a novel method for examining multistable structures during the testing stage of the design process. One force transducer and multiple velocity transducers are placed at various locations on a multistable structure. In fact, any displacement or acceleration sensor may also be used, so long as appropriately integrated or differentiated data processing methods are undertaken to transform the response into a velocity data stream. The measurements from these sensors are then used

to calculate the impedance of the structure in real time at each point a velocity transducer is located. If a velocity transducer is placed at the location of the force transducer, the onset of bifurcations and nonlinear resonances is governed by the trends observed for drive point impedances, while a velocity transducer placed elsewhere is governed by the trends observed for transfer impedances. This would provide a powerful new tool for experimentally evaluating the dynamic sensitivities of multistable structures, such as post-buckled aircraft panels, before full system integration.

This research lays the groundwork for future investigations into how impedance measurements of built-up, multistable structures inform the dynamic behavior of post-buckled constituents. Future work will involve numerical simulations of the governing equations of motion in order to determine how system parameters such as degree of buckling and linear coupling stiffness impact the impedance measurements of system sub-components in order to provide general design decision guidelines. Characterization of the roles of coupled physics, such as thermal stresses, will uncover how the multiphysics environment of hypersonic flight contributes to the complex, nonlinear response behaviors of multistable structures.

6 BIBLIOGRAPHY

[1] C. F. Ng and S. A. Clevenson, "High-Intensity Acoustic Tests of a Thermally Stressed Plate," *Journal of Aircraft,* vol. 28, no. 4, pp. 275-281, 1991.

[2] G. Houston, D. Quinn, A. Murphy and F. Bron, "Wing Panel Design with Novel Skin-Buckling Containment Features," *Journal of Aircraft,* vol. 53, no. 2, pp. 416-426, 2016.

[3] D. Quinn, A. Murphy and L. Cervi, "Fatigue performance of aircraft panels with novel skin buckling containment features," *Journal of Aerospace Engineering,* vol. 225, pp. 791-806, 2011.

[4] Lockheed Martin, "Creating The Blackbird," [Online]. Available: http://www.lockheedmartin.com/us/100years/stories/blackbird.html.

[5] Boeing, "B-52," [Online]. Available: http://www.boeing.com/defense/b-52-bomber.

[6] L. Virgin, Introduction to Experimental Nonlinear Dynamics, Cambridge: Cambridge University Press, 2000.

[7] R. L. Harne and B. A. Goodpaster, "in review," 2016.

[8] F. Fahy and J. Walker, Advanced Applications in Acoustics, Noise, and Vibration, New York: Spon Press, 2004.

[9] J. V. Ferreira and D. J. Ewins, "Nonlinear receptance coupling approach based on describing functions," in *Proceedings of the 14th International Modal Analysis Conference (IMAC XIV)*, Dearborn, Michigan, USA, 1996.

[10] R. W. Clough and E. L. Wilson, "Dynamic analysis of large structural systems with local nonlinearities," *Computer Methods in Applied Mechanics and Engineering,* vol. 17/18, pp. 107-129, 1979.

[11] H. Elizalde and M. Imregun, "An explicit frequency response function formulation for multi-degree-of-freedom non-linear systems," *Mechanical Systems and Signal Processing,* vol. 20, pp. 1867-1882, 2006.

[12] O. Tanrikulu and M. Imregun, "Forced harmonic response analysis of nonlinear structures using describing functions," *AIAA Journal,* vol. 31, pp. 1313-1320, 1993.

[13] R. Wiebe, L. N. Virgin, I. Stanciulescu, S. M. Spottswood and T. G. Eason, "Characterizing Dynamic Transitions Associated With Snap-Through: A Discrete System," *Journal of Computational and Nonlinear Dynamics,* vol. 8, no. 1, p. 11010, 2012.

[14] L. Virgin, "The dynamics of symmetric post-buckling," *International Journal of Mechanical Sciences,* vol. 27, pp. 235-248, 1985.

[15] R. Harne and K. Wang, Harnessing Bistable Structural Dynamics: for Vibration Control, Energy Harvesting and Sensing, Chichester: John Wiley & Sons Ltd., 2017.

[16] S. Spottswood, T. Eason and R. Chona, "A structural perspective on the challenges associated with analyzing a reusable hypersonic platform," in *Proceedings of the 11th International Conference on Recent Advancements on Structural Dynamics*, Pisa, Italy, 2013.

[17] S. Sridharan and M. Peng, "Performance of Axially Compressed Stiffened Panels," *International Journal of Solids and Structures,* vol. 25, no. 8, pp. 879-899, 1989.

[18] S. Spottswood and R. Allemang, "Identification of nonlinear parameters for reduced order models," *Journal of Sound and Vibration,* vol. 295, pp. 226-245, 2006.

[19] S. Spottswood and R. Allemang, "On the investigation of some parameter identification and experimental modal filtering issues for nonlinear reduced order models," *Experimental Mechanics,* vol. 47, pp. 511-521, 2007.

[20] A. delli Carri and D. Ewins, "A systematic approach to modal testing of nonlinear structures," in *Topics in Modal Analysis Volume 7: Proceedings of the 31st IMAC Conference on Structures Dynamics*, R. Allemang, J. De Clerck, C. Niezrecki and A. Wicks, Eds., New York, Springer, 2014, pp. 273-286.

[21] R. Wiebe and S. Spottswood, "On the dimension of complex responses in nonlinear structural vibrations," *Journal of Sound and Vibration,* vol. 373, pp. 192-204, 2016.

[22] B. Miller, J. McNamara, S. Spottswood and A. Culler, "The impact of flow induced loads on snap-through behavior of acoustically excited, thermally buckled panels," *Journal of Sound and Vibration,* vol. 330, pp. 5736-5752, 2011.

[23] A. Culler and J. McNamara, "Studies on fluid-thermal-structural coupling for aerothermoelasticity in hypersonic flow," *AIAA Journal,* vol. 48, pp. 1721-1738, 2010.

[24] W. Palm, System Dynamics, New York: McGraw-Hill, 2014.

[25] J. Collins, H. Busby and G. Staab, Mechanical Design of Machine Elements and Machines: A Failure Prevention Perspective, John Wiley & Sons, Inc., 2010.

7 APPENDIX

7.1 Sample MATLAB code

Below is a sample of the MATLAB code, which uses the data acquisition toolbox to record analog input signals from the five sensors and then post-processes the data in order to generate frequency response, amplitude response, and impedance plots.

```
%% acquire data?
dataacquire=1; % yes for acquire

%% experimental setup parameters
d.test_name='base_acceleration_frequency_sweep'; % type of excitation
delivered to beam

%% post-processing relevant parameters
% test types are:
% 'sine' which is either frequency sweep or constant-frequency sinusoid
% 'random' which is random excitation
% 'ring-down' which are impulses on test components, used to determine
natural frequencies and damping ratios
% NOTE: each test may require a modified hi and lo frequency cutoff set for
the digital filtering
d.test_type='sine';

%% data acquisition setup parameters
d.fs=2048; % sampling frequency [Hz]
d.wind=@hann; % window type for averages
d.seconds=810; % [s] seconds of data acquisition, determined according to
Vibration Research VR9500 controller test setup
d.filter_data_lo=1; % [Hz] of high pass cut off frequency
d.filter_data_hi=200; % [Hz] of low pass cut off frequency

%% fft computation parameters
% for 'sine' and 'random' tests only
% TIME_SAMPLED_PER_FFT is very important towards quality of post-processed
% data. If first attempt is not so great, try greater and lesser values.
d.time_sampled_per_fft=5; % [s] seconds of data acquisition over which fft is
evaluated
d.spacing_cts=round(d.fs*d.time_sampled_per_fft); % number of samples to use
in FFT to obtain freq_spacing
d.fft_numbers=floor(d.fs*d.seconds/d.spacing_cts); % number of ffts to
compute/loop through
d.nft=2^nextpow2(d.spacing_cts); % number of samples next to power of 2 for
spacing_cts

%% filename for save d structure
c=clock; % grab the time-stamp, eliminates possibility of data overwrite
d.filename=[num2str(c(1)) '_' num2str(c(2),'%02.0f') '_'
num2str(c(3),'%02.0f') '_' num2str(c(4),'%02.0f') num2str(c(5),'%02.0f')
'_multistable_beam_system_' d.test_name '.mat'];
saveon=1; % save the data?

%% sensor sensitivity
```

```
d.sensor{1}='PCB_333B40_SN_57722_accelerometer_on_shaker_with_VR9500_controll
er';
d.sensor{2}='PCB_208C01_SN_LW42544_force_transducer_on_shaker';
d.sensor{3}='PCB_352A24_SN_LW211074_accelerometer_on_beam_1';
d.sensor{4}='PCB_352A24_SN_LW211081_accelerometer_on_beam_2';
d.sensor{5}='PCB_352A24_SN_LW211082_accelerometer_on_beam_3';
d.ch_sens(1)=1/.0527; % (m/s^2)/V  % PCB 333B40 accelerometer
d.ch_sens(2)=1/.1161; % N/V % PCB 208C01 force transducer
d.ch_sens(3)=1/.01084; % (m/s^2)/V  % PCB 352A24 accelerometer
d.ch_sens(4)=1/.01005; % (m/s^2)/V  % PCB 352A24 accelerometer
d.ch_sens(5)=1/.01007; % (m/s^2)/V  % PCB 352A24 accelerometer

%% mean sensor values [V] for each channel, to be subtracted from the input
before sensitivity to [units]
d.data_mean(1)=0; %
d.data_mean(2)=0; %
d.data_mean(3)=0; %
d.data_mean(4)=0; %
d.data_mean(5)=0; %

%% if for data acquisition
if dataacquire==1 % 1=yes for acquire

%% identify connected devices
devices=daq.getDevices;
% once obtained, ensure using correct device name in below session and
acquire lines

%% acquire data
s=daq.createSession('ni');
s.addAnalogInputChannel('Dev3',0,'Voltage'); % add input channels
s.addAnalogInputChannel('Dev3',1,'Voltage');
s.addAnalogInputChannel('Dev3',2,'Voltage');
s.addAnalogInputChannel('Dev3',3,'Voltage');
s.addAnalogInputChannel('Dev3',4,'Voltage');
s.Rate=d.fs; % set output and measuring frequency [Hz]
s.DurationInSeconds=d.seconds; % [s] duration of data acquisition
[d.data,d.time_series]=s.startForeground;
d.nn_chan=min(size(d.data));

%% bandpass filter data
clear ch_f
d.nn_chan=min(size(d.data));
%
myfilt=designfilt('lowpassiir','filterorder',4,'passbandfrequency',d.filter_d
ata_hi,'PassbandRipple',0.01,'samplerate',d.fs);
myfilt=designfilt('bandpassiir','filterorder',4,'HalfPowerFrequency1',d.filte
r_data_lo,'HalfPowerFrequency2',d.filter_data_hi,'samplerate',d.fs);
for iii=1:d.nn_chan
ch_f(:,iii)=filtfilt(myfilt,d.ch_sens(iii)*(d.data(:,iii)-d.data_mean(iii)));
%
end

%%
end
```

```
%%
d.data_filt=ch_f; % re-assign filtered data from local to structure variable

%% post-process data
%%
if strcmp(d.test_type,'sine')==1
%%
clear ch_ft gxy gxx coh tf y tf_here_est tf_here_gxy
d.inst_mean=[];d.f_ft=[];d.meansq=[];d.corr=[];d.lags=[];d.ch_ft_instavg=[];d
.freq_instavg=[];d.gxx_instavg=[];d.gxy_instavg=[];d.tf_here_est=[];d.tf_here
_gxy=[];
for ooo=1:2*d.fft_numbers-1 %  1:d.fft_numbers for no overlap.
1:2*d.fft_numbers-1 with half-overlap as defined below in trunc
    %     trunc=(ooo-1)*d.spacing_cts+1:ooo*d.spacing_cts; % define
truncation in time : no overlap in averaging
    trunc=(ooo-1)*d.spacing_cts/2+1:ooo*d.spacing_cts/2+d.spacing_cts/2; %
define truncation in time : gives half-overlap of windowed averages is the
ooo=1:2*d.fft_numbers-1
    for iii=1:d.nn_chan
    d.inst_mean(ooo,iii)=mean(d.data_filt(trunc,iii)); % mean of
instantaneous data stream for the channel

y(:,iii)=fft(d.data_filt(trunc,iii).*window(d.wind,length(trunc)),d.nft)/(d.s
pacing_cts*mean(window(d.wind,length(trunc))));
%     y(:,iii)=fft(d.data_filt(trunc,iii),d.nft)/(d.spacing_cts); % take fast
fourier transform of data
    ch_ft(:,iii,ooo)=2*abs(y(1:d.nft/2+1,iii)); % magnitude of single-sided
fourier transform
    d.f_ft=d.fs/2*linspace(0,1,d.nft/2+1)'; % define frequency vector
    gxx(:,iii,ooo)=y(:,iii).*conj(y(:,iii))/2; % auto power spectrum
    if iii>1
    gxy(:,iii,ooo)=y(:,iii).*conj(y(:,2))/2; % cross power spectrum,
referencing input force

tf_here_est(:,iii,ooo)=tfestimate(d.data_filt(trunc,2),d.data_filt(trunc,iii)
,[],[],d.nft,d.fs); % MATLAB estimate transfer function of signal to force
    tf_here_gxy(:,iii,ooo)=y(:,2)./y(:,iii);gxy(:,iii,ooo)./gxx(:,2,ooo); %
direct computation of transfer function of signal to force, tends to be of
coarser resolution than MATLAB estimate
    end
    d.meansq(iii,ooo)=mean((d.data_filt(trunc,iii)-d.inst_mean(ooo,iii)).^2);
% mean-square system response [units]^2, with mean eliminated
    [d.corr(:,iii,ooo),d.lags]=xcorr(d.data_filt(trunc,iii)-
d.inst_mean(ooo,iii),d.data_filt(trunc,iii)-d.inst_mean(ooo,iii),'unbiased');
% autocorrelation of the signal
    end

%     figure(23);clf;plot(d.f_ft,squeeze(ch_ft(:,1,ooo)));xlim([5
150]);drawnow;

    [mmx,ind]=max(squeeze(ch_ft(5:end,1,ooo))); % grab max and location of
max for first channel, control accelerometer, to identify the instantaneous
frequency [Hz]
    % the above look forward by 4 indices is to eliminate potential for high
DC component (due to signal shift) which will mislead results
```

```
    ind=ind+4; % look forward to accommodate above processing
    d.freq_instavg(ooo)=d.f_ft(ind); % [Hz] mean instantaneous excitation
frequency
    d.ch_ft_instavg(ooo,:)=max(squeeze(ch_ft(ind-2:ind+2,:,ooo)),[],1); % the
signals' FFT amplitude at this instantaneous frequency [units]
    d.gxx_instavg(ooo,:)=max(squeeze(gxx(ind-2:ind+2,:,ooo)),[],1); % the
signals' autospectral density at this instantaneous frequency [units^2]
    d.gxy_instavg(ooo,:)=max(squeeze(gxy(ind-2:ind+2,:,ooo)),[],1); % the
signals' cross spectral density at this instantaneous frequency [units^2]
    indt=ind; % hold index
    for rrr=2:5
    [tmax,ind]=max(squeeze(abs(tf_here_est(indt-2:indt+2,rrr,ooo))),[],1); %
find maximum index for tf

d.tf_here_est(ooo,rrr)=1./(1./j./(2*pi*d.freq_instavg(ooo)).*squeeze(tf_here_
est(ind+indt,rrr,ooo))); % signals' transfer function impedance estimated by
MATLAB

d.tf_here_est(ooo,rrr)=1./(1./j./(2*pi*d.freq_instavg(ooo)).*squeeze(tf_here_
est(indt,rrr,ooo))); % signals' transfer function impedance estimated by
MATLAB
    [tmax,ind]=max(squeeze(abs(tf_here_gxy(indt-2:indt+2,rrr,ooo))),[],1); %
find maximum index for tf

d.tf_here_gxy(ooo,rrr)=1./(1./j./(2*pi*d.freq_instavg(ooo)).*squeeze(tf_here_
gxy(ind+indt,rrr,ooo))); % signals' transfer function impedance determined by
direct computation, tends to be of coarser accuracy than MATLAB estimate

d.tf_here_gxy(ooo,rrr)=(1*2*pi*d.freq_instavg(ooo)).*squeeze(tf_here_gxy(indt
,rrr,ooo)); % signals' transfer function impedance determined by direct
computation, tends to be of coarser accuracy than MATLAB estimate
    end
end
%%
% close 23
%% plot
close all
colors=['r' 'g' 'b' 'c' 'm' 'k'];
markers=['o' 's' 'v' 'd' '^' 'x'];

red_range=5; % index to plot in from full extent of frequencies
flims=[10 30]; % [Hz] frequency limits for plotting

figure(1);
clf;
for rrr=1:3
plot(d.freq_instavg(red_range:end-red_range+1),d.ch_ft_instavg(red_range:end-
red_range+1,rrr+2)./(2*pi*d.freq_instavg(red_range:end-
red_range+1)'),[colors(rrr) markers(rrr) '-'])
hold on
end
xlabel('frequency [Hz]');
xlim(flims)
% ylabel('acceleration [m/s2]');
ylabel('velocity [m/s]');
% set(gca,'yscale','log')
```

```
% ylim([5e-5 5e-1]);
box on
title({[strrep(d.filename,'_','-')],['mean base accel '
num2str(mean(d.ch_ft_instavg(:,1)),'%1.3f') 'm/s2. mean force '
num2str(mean(d.ch_ft_instavg(:,2)),'%1.4f') 'N. rgb beams123']})
% savefig([strrep(d.filename,'.mat','') '_velocity_amplitudes.fig'])

% amplitude respone
figure(124);
clf;
for rrr=1:3
    plot(d.ch_ft_instavg(red_range:end-
red_range+1,1),d.ch_ft_instavg(red_range:end-
red_range+1,rrr+2)./(2*pi*d.freq_instavg(red_range:end-
red_range+1)'),[colors(rrr) markers(rrr) '-'])
    hold on
end
hold off
freq_level = 22; %[Hz]
xlabel('input acceleration [m/s^2]');
ylabel('beam velocity [m/s]');
title({[strrep(d.filename,'_','-')],['excitation frequency '
num2str(d.freq_instavg(1),'%1.3f') 'Hz. rgb beams123']})
% amp_sweep_title = [figure_title,' ; ',num2str(freq_level),' Hz'];
% title(amp_sweep_title);
box on

for rrr=1:3
figure(1+rrr);
clf;
semilogy(d.freq_instavg(red_range:end-
red_range+1),abs(d.tf_here_gxy(red_range:end-red_range+1,rrr+2)),[colors(rrr)
markers(rrr) '-'])
xlabel('frequency [Hz]');
xlim(flims)
ylabel({['transfer function, impedance'],['amplitude [N/(m/s)]']});
box on
title({[strrep(d.filename,'_','-')],['beam ' num2str(rrr) '. mean base accel
' num2str(mean(d.ch_ft_instavg(:,1)),'%1.3f') 'm/s2. mean force '
num2str(mean(d.ch_ft_instavg(:,2)),'%1.4f') 'N']})
% savefig([strrep(d.filename,'.mat','') '_impedance_amplitude_beam_'
num2str(rrr) '.fig'])

% figure(4+rrr);
% clf;
% plot(d.freq_instavg(red_range:end-
red_range+1),180/pi*(angle(d.tf_here_est(red_range:end-
red_range+1,rrr+2))),[colors(rrr) markers(rrr) '-'])
% xlabel('frequency [Hz]');
% xlim(flims)
% ylabel({['transfer function, impedance'],['phase [degrees]']});
% box on
% title({[strrep(d.filename,'_','-')],['beam ' num2str(rrr) '. mean base
accel ' num2str(mean(d.ch_ft_instavg(:,1)),'%1.3f') 'm/s2. mean force '
num2str(mean(d.ch_ft_instavg(:,2)),'%1.4f') 'N']})
```

```
% savefig([strrep(d.filename,'.mat','') '_impedance_phase_beam_' num2str(rrr)
'.fig'])

figure(7+rrr);
clf;
plot(real(d.tf_here_gxy(red_range:end-
red_range+1,rrr+2)),imag(d.tf_here_gxy(red_range:end-
red_range+1,rrr+2)),[colors(rrr) markers(rrr) '-
'],real(d.tf_here_est(3,rrr+2)),imag(d.tf_here_est(3,rrr+2)),'x',real(d.tf_he
re_est(round(end/2),rrr+2)),imag(d.tf_here_est(round(end/2),rrr+2)),'+')
jump=15;
indr=min(find(real(d.tf_here_gxy(jump:end-jump,rrr+2))<=0));
indi=min(find(imag(d.tf_here_gxy(jump:end-jump,rrr+2))<=0));
hold on;
text(real(d.tf_here_gxy(indr+jump-1,rrr+2)),imag(d.tf_here_gxy(indr+jump-
1,rrr+2)),[num2str(d.freq_instavg(indr+jump-1),'%1.1f') ' Hz']);
text(real(d.tf_here_gxy(indi+jump-1,rrr+2)),imag(d.tf_here_gxy(indi+jump-
1,rrr+2)),[num2str(d.freq_instavg(indi+jump-1),'%1.1f') ' Hz']);
xlabel('real impedance, resistance [N.s/m]');
ylabel('imaginary impedance, reactance [N.s/m]');
box on
title({[strrep(d.filename,'_','-')],['rgb. beams12' num2str(rrr) '. mean base
accel ' num2str(mean(d.ch_ft_instavg(:,1)),'%1.3f') 'm/s2. mean force '
num2str(mean(d.ch_ft_instavg(:,2)),'%1.4f') 'N. x starts and + is halfway']})
% savefig([strrep(d.filename,'.mat','') '_impedance_real_imag_beam_'
num2str(rrr) '.fig'])

figure(10+1);
% clf;
plot(d.freq_instavg(red_range:end-
red_range+1),real(d.tf_here_gxy(red_range:end-
red_range+1,rrr+2)),[colors(rrr) markers(rrr) '-']);
hold on
xlabel('frequency [Hz]');
xlim(flims)
ylabel({['transfer function, real impedance'],['resistance [N/(m/s)]']});
box on
title({[strrep(d.filename,'_','-')],['rgb. beams12' num2str(rrr) '. mean base
accel ' num2str(mean(d.ch_ft_instavg(:,1)),'%1.3f') 'm/s2. mean force '
num2str(mean(d.ch_ft_instavg(:,2)),'%1.4f') 'N']})
% savefig([strrep(d.filename,'.mat','') '_impedance_real_beams123.fig'])

figure(13+1);
% clf;
plot(d.freq_instavg(red_range:end-
red_range+1),imag(d.tf_here_gxy(red_range:end-
red_range+1,rrr+2)),[colors(rrr) markers(rrr) '-']);
hold on
xlabel('frequency [Hz]');
xlim(flims)
ylabel({['transfer function, imaginary impedance'],['reactance [N/(m/s)]']});
box on
title({[strrep(d.filename,'_','-')],['rgb. beam ' num2str(rrr) '. mean base
accel ' num2str(mean(d.ch_ft_instavg(:,1)),'%1.3f') 'm/s2. mean force '
num2str(mean(d.ch_ft_instavg(:,2)),'%1.4f') 'N']})
% savefig([strrep(d.filename,'.mat','') '_impedance_imag_beams123.fig'])
```

```
end

%%
end
%%
%%
if strcmp(d.test_type,'random')==1
%%
clear ch_ft gxy gxx coh tf y
d.inst_mean=[];d.f_ft=[];d.ch_ft_a=[];d.gxx_a=[];d.gxy_a=[];
for ooo=1:2*d.fft_numbers-1 %  1:d.fft_numbers for no overlap.
1:2*d.fft_numbers-1 with half-overlap as defined below in trunc
%     trunc=(ooo-1)*d.spacing_cts+1:ooo*d.spacing_cts; % define truncation in
time : no overlap in averaging
    trunc=(ooo-1)*d.spacing_cts/2+1:ooo*d.spacing_cts/2+d.spacing_cts/2; %
define truncation in time : gives half-overlap of windowed averages is the
ooo=1:2*d.fft_numbers-1
    for iii=1:d.nn_chan
    d.inst_mean(ooo,iii)=mean(d.data_filt(trunc,iii)); % mean of
instantaneous data stream for the channel

y(:,iii)=fft(d.data_filt(trunc,iii).*window(d.wind,length(trunc)),d.nft)/(d.s
pacing_cts*mean(window(d.wind,length(trunc))));
    ch_ft(:,iii,ooo)=2*abs(y(1:d.nft/2+1,iii)); % magnitude of single-sided
fourier transform
    d.f_ft=d.fs/2*linspace(0,1,d.nft/2+1)'; % define frequency vector
    gxx(:,iii,ooo)=y(:,iii).*conj(y(:,iii))/2; % auto power spectrum
    if iii>1
    gxy(:,iii,ooo)=y(:,2).*conj(y(:,iii))/2; % cross power spectrum,
referencing input force
    end
    end

    figure(23);clf;semilogy(d.f_ft,squeeze(ch_ft(:,1,ooo)));xlim([5
250]);drawnow;

end

for iii=1:d.nn_chan
d.ch_ft_a(:,iii)=mean(squeeze(ch_ft(1:d.nft/2+1,iii,:)),2); % average fft of
signal
d.gxx_a(:,iii)=mean(squeeze(gxx(1:d.nft/2+1,iii,:)),2); % average
autospectrum of signal
d.gxy_a(:,iii)=mean(squeeze(gxy(1:d.nft/2+1,iii,:)),2); % average
autospectrum of signal
end

%%
close 23
%% plot
figure(1);
clf;
hold on
semilogy(d.f_ft,d.ch_ft_a(:,3),'r');%./d.ch_ft_a(:,2),'o')
semilogy(d.f_ft,d.ch_ft_a(:,4),'g');%./d.ch_ft_a(:,2),'o')
```

```
semilogy(d.f_ft,d.ch_ft_a(:,5),'b');%./d.ch_ft_a(:,2),'o')
% semilogx(d.ch_ft_instavg(:,1),d.ch_ft_instavg(:,3:5),'o')
xlabel('frequency [Hz]');
% xlabel('input force amplitude [N]')
% xlabel('base acceleration [m/s2]');
xlim([5 150])
ylabel('acceleration [m/s2]');
set(gca,'yscale','log')

%%
end

%%
%%
if strcmp(d.test_type,'ring-down')==1
%%
clear ch_ft gxy gxx coh tf y
% identify start and stop times
ind1=max(find(d.time_series<=34.5));
ind2=max(find(d.time_series<=35));
trunc=ind1:ind2;
d.nft=2^nextpow2(length(trunc)); % number of samples next to power of 2 for
spacing_cts
window_hold=exp(-4*[1:length(trunc)]'/d.fs);
for iii=1:d.nn_chan
%
y(:,iii)=fft(d.data_filt(trunc,iii).*window(d.wind,length(trunc)),d.nft)/(len
gth(trunc)*mean(window(d.wind,length(trunc))));

y(:,iii)=fft(d.data_filt(trunc,iii).*window_hold,d.nft)/(length(trunc)*mean(w
indow_hold));
    ch_ft(:,iii)=2*abs(y(1:d.nft/2+1,iii)); % magnitude of single-sided
fourier transform
    d.f_ft=d.fs/2*linspace(0,1,d.nft/2+1)'; % define frequency vector
end
d.f_ft=d.fs/2*linspace(0,1,d.nft/2+1)'; % define frequency vector
figure(23);
clf;
plot(d.f_ft,ch_ft(:,3:5))
xlabel('frequency [Hz]');
ylabel('fft [units]');
xlim([5 100]);

%% use cursor info on figure to highlight increasing time successive peaks
% or minima. and name the cursor info export to workspace cs
clear freq drat dec;
for iii=1:(length(cs)-1)
    freq(iii)=1./(cs(iii).Position(1)-cs(iii+1).Position(1));
    dec(iii)=log(cs(iii).Position(2)/cs(iii+1).Position(2));
    drat(iii)=1./sqrt(1+(2*pi/dec(iii))^2);
end
disp(['nat freqq ' num2str(mean(freq),'%1.4f') ' Hz. damping ratio '
num2str(mean(drat),'%1.5f') ]);

%%
%% plot
```

```
%%
end

%%

%% save data
if saveon==1
    d.data_filt=[];
    d.inst_mean=[];
    d.meansq=[];
    d.corr=[];
    d.lags=[];
    d.tf_here_est=[];
    d.tf_here_gxy=[];
    save(d.filename,'d');
end
```